A HIGHLY COMPLETE SPECTROSCOPIC SURVEY OF THE GOODS-N FIELD[1,2,3]

A. J. Barger,[4,5,6] L. L. Cowie,[6] and W.-H. Wang[7,8]

ABSTRACT

We present a table of redshifts for 2907 galaxies and stars in the 145 arcmin^2 *HST* ACS GOODS-North, making this the most spectroscopically complete redshift sample obtained to date in a field of this size. We also include the redshifts, where available, in a table containing just under 7000 galaxies from the ACS area with $K_{s, \mathrm{AB}} < 24.5$ measured from a deep K_s image obtained with WIRCam on the CFHT, as well as in a table containing 1016 sources with $\mathrm{NUV_{AB}} < 25$ and 478 sources with $\mathrm{FUV_{AB}} < 25.5$ (there is considerable overlap) measured from the deep *GALEX* images in the ACS area. Finally, we include the redshifts, where available, in a table containing the 1199 24 μm sources to 80 μJy measured from the wider area *Spitzer* GOODS-North. The redshift identifications are greater than 90% complete to magnitudes of F435W$_{\mathrm{AB}} = 24.5$, F850LP$_{\mathrm{AB}} = 23.3$, and $K_{s, \mathrm{AB}} = 21.5$, and to 24 μm fluxes of 250 μJy. An extensive analysis of these data appear in a companion paper, but here we test the efficiency of color-selection techniques to identify populations of high-redshift galaxies and active galactic nuclei. We also examine the feasibility of doing tomography of the intergalactic medium with a 30 m telescope.

Subject headings: cosmology: observations — galaxies: active — galaxies: distances and redshifts — galaxies: evolution — galaxies: formation

Online material: machine-readable tables

1. INTRODUCTION

Substantial progress has been made in tracing the formation and evolution of galaxies through extensive multiwavelength observations of extragalactic survey fields. However, the most challenging and time-consuming task is spectroscopically identifying the sources. This is especially true when one is trying to identify complete samples to faint magnitude limits. Although with existing multiwavelength data sets we can construct spectral energy distributions (SEDs) and measure photometric redshifts for galaxies, spectra provide an enormous amount of additional information on the sources. We have therefore carried out a very high quality, nearly spectroscopically complete, magnitude-limited redshift survey of the Great Observatories Origins Deep Survey–North (GOODS-N; Giavalisco et al. 2004) field. The GOODS-N is one of the most intensively studied regions in the sky, and in many bandpasses it has the deepest images ever obtained. It has also been the target of extensive spectroscopic observations over the years (e.g., Cohen et al. 2000; Wirth et al. 2004; Cowie et al. 2004). Thus, it is nearly ideal for the present study.

In a companion paper (Cowie & Barger 2008) we use this unique spectral database to place galaxies into the overall evolutionary scheme by combining spectral line and break diagnostics with colors and by analyzing metal evolution. Here we present the data catalogs and use the redshift information to test the efficiency of using color-selection techniques to identify populations of high-redshift galaxies and active galactic nuclei (AGNs). We also determine which AGNs can be distinguished by their colors. We then use the data set to examine the feasibility of doing intergalactic medium (IGM) tomography on a 30 m telescope.

Techniques have been developed to preselect high-redshift candidates for spectroscopic confirmation using simple photometric selection criteria. The Lyman break galaxy (LBG) dropout technique (e.g., Cowie et al. 1988; Songaila et al. 1990; Lilly et al. 1991; Steidel & Hamilton 1993; Steidel et al. 1995) is the most heavily used of these and has really opened up the field to the study of $z > 3$ star-forming galaxies. However, with the advent of wide-area near-infrared (NIR) arrays, other selections, including the distant red galaxy (DRG) color selection (Franx et al. 2003; van Dokkum et al. 2003; $z \gtrsim 2$) and the *BzK* color selection (Daddi et al. 2004; $1.4 \lesssim z \lesssim 2.5$), have recently become popular. The above selections are, of course, limited to sources that can be observed in optical and NIR surveys, but they have produced a substantial sample of spectroscopically confirmed high-redshift galaxies and AGNs. H^- methods using the mid-infrared (MIR) spectral shapes have also been suggested (e.g., Simpson & Eisenhardt 1999; Sawicki 2002). Although these techniques have not been heavily used, they are of considerable interest for optically faint sources.

With all of these avenues for finding high-redshift sources, we would hope that there are not still significant populations that remain unidentified. Recently, however, Le Fèvre et al. (2005) and Paltani et al. (2007) have challenged this view using the VIMOS Very Large Telescope Deep Survey (VVDS), a purely *I* flux-selected sample (targets have magnitudes between $I_{\mathrm{AB}} = 17.5$ and 24) of 9295 galaxies ("first epoch") with measured redshifts in the range $0 \leq z \leq 5$. These authors claim surface densities

consistently larger than those of Steidel et al. (1996, 1999, 2004) by factors of 1.6–6.2 at $z \approx 3$, with the largest factor applying to the brightest magnitudes. In calculating the surface densities, they corrected for the fraction of galaxies they did not observe ($\sim$76%) and for their estimate of the fraction of galaxies with incorrect redshifts. The need for the latter correction arises from their use of redshifts with all four of their reliability flags (flags 3 and 4 have very reliable measurements; flag 2 has a reasonably reliable measurement, but there is a nonnegligible probability that the redshift is wrong; flag 1 has a tentative measurement, but there is a significant probability that the redshift is wrong). They concluded that the LBG selection techniques and photometric redshift studies are not able to identify the full population of high-redshift galaxies found through spectroscopic observations of pure magnitude-selected samples. This claim requires verification from a highly spectroscopically complete sample with very reliable redshift identifications.

A 30 m telescope will revolutionize wide-field spectroscopy, making sources that are currently 10 times too faint for moderate-to-high dispersion spectroscopy in the optical accessible and mapping the distribution of galaxies over the redshift range $2 \leq z \leq 4$. Of most interest, however, is whether a 30 m telescope will allow dense sampling of the IGM through the use of background galaxies. This would be an enormous improvement over the one-dimensional information now obtained through the study of rare high-redshift quasars, whose surface density on the sky at magnitudes accessible with Keck is very low. To trace the three-dimensional distribution of diffuse gas at high redshifts would require a high density of background probes, but it needs to be determined whether the necessary surface density of such probes exists.

The structure of the paper is as follows. In §§ 2 and 3 we describe, respectively, our photometry and our spectroscopy. In § 4 we examine how well different color selection techniques do, including LBG selection in § 4.1, BzK selection in § 4.2, and H$^-$ selection in § 4.3. In § 5 we consider whether IGM tomography is feasible with a 30 m telescope, and in § 6 we summarize our results.

We assume $\Omega_M = 0.3$, $\Omega_\Lambda = 0.7$, and $H_0 = 70 \ \mathrm{km \ s^{-1} \ Mpc^{-1}}$ throughout. All magnitudes are given in the AB magnitude system, where an AB magnitude is defined by $m_{AB} = -2.5 \log f_\nu - 48.60$. Here f_ν is the flux of the source in units of ergs cm^{-2} s^{-1} Hz^{-1}.

2. THE PHOTOMETRIC DATA

2.1. Optical Imaging

We take the optical photometric data from existing work. In particular, we take the U magnitudes from Capak et al. (2004) and the F435W, F606W, F775W, and F850LP magnitudes from the *HST* Advanced Camera for Surveys (ACS) observations of the GOODS-N (Giavalisco et al. 2004). There is an absolute offset in declination of 0.4″ from the 20 cm Very Large Array (VLA)[9] image of Richards (2000) to the ACS and *Spitzer* images, so we applied a −0.4″ offset to the ACS and *Spitzer* catalogs to make them consistent with the ground-based optical and NIR data and the X-ray and radio data, all of which are already in the VLA astrometric frame. All coordinates in the tables are given in the VLA astrometric frame.

2.2. Near-Infrared Imaging

We have obtained new ultradeep K_s images from the Wide-field Infrared Camera (WIRCam) on the CFHT 3.6 m telescope

and from the Multi-Object Infrared Camera and Spectrograph (MOIRCS) on the Subaru 8.2 m telescope. WIRCam covers the entire ACS and *Spitzer* GOODS-N regions in one pointing. The WIRCam image is a $\sim$40 hr exposure and reaches a 5 σ limit of $K_{s, AB} = 24.8$. MOIRCS has a smaller field of view, but we obtained an ultradeep mosaic that covers nearly the full ACS area after including all available data in the Subaru archive. The MOIRCS image has a very nonuniform sensitivity distribution, but the image quality is extremely good (0.4″–0.5″ throughout). Although we cross-compared the WIRCam image with the MOIRCS image to eliminate artifacts and fragments of larger galaxies in constructing the catalogs, we measured the K_s-band magnitudes from the WIRCam image alone. Below we describe the WIRCam and MOIRCS observations and data reduction.

2.2.1. WIRCam Imaging

WIRCam consists of four 2k × 2k HAWAII2-RG detectors covering a field of view of 20′ × 20′ with a 0.3″ pixel scale. K_s-band imaging observations were carried out by our group in semesters 2006A and 2007A and by a Canadian group led by Luc Simard in 2006A. The images were dithered to cover the detector gap and to obtain a uniform sensitivity distribution. Most of the observations were performed under photometric conditions with seeing between 0.6″ and 1″, and the total integration time was 39.7 hr.

The data were reduced in IDL using the SIMPLE Imaging and Mosaicking Pipeline (SIMPLE; W.-H. Wang 2008, in preparation).[10] Images within a dither set (typically 15 minutes in length) were flattened using an iterative median sky flat in which a simple median sky was first derived to flatten the images and then a second median sky was derived by masking all of the detected objects using the flattened images. After the images were flattened, the residual sky background was subtracted from each image with a smooth polynomial surface fitted to the masked image. Crosstalk effects between each of the 32 readout channels on a detector were removed by subtracting the median of the 32 64 × 2k channels in the object-masked image. This removes most of the crosstalk, and only weak residual features persist around the few brightest stars in the field. The small areas contaminated by the residual crosstalk are mostly outside the ACS and *Spitzer* GOODS-N regions and are excluded in this work. The brightest cosmic-ray hits were removed by a 5 × 5 pixel sigma filtering in each flattened image.

We used the SExtractor package (Bertin & Arnouts 1996) to measure the object positions and fluxes in each flattened, sky-subtracted, and crosstalk-removed image in a dither set. The first-order derivative of the optical distortion function was derived by measuring the offsets of each object in the dither sequence as a function of location in the images. Absolute astrometry was obtained by matching the detected objects to a reference catalog constructed with brighter and compact objects in the ACS catalog (Giavalisco et al. 2004; after correcting for the 0.4″ offset between the ACS and radio frames) and the SuprimeCam catalog (Capak et al. 2004). The reduced exposures were then warped directly from the raw frames to a common tangential sky plane with a subpixel accuracy. This projection corrects for both optical distortion and absolute astrometry. All projected images were weighted by their sky transparencies and exposure times and were combined to form a large mosaic. When images from a dither set were combined, a sigma filter was applied to pixels that have the same sky position to further remove fainter cosmic rays and artifacts such as reflections inside the optics. In the image combination the SExtractor

---

[9] The VLA is operated by the National Radio Astronomy Observatory, which is a facility of the National Science Foundation, operated under cooperative agreement by Associated Universities, Inc.

[10] See also http://www.aoc.nrao.edu/~whwang/idl/SIMPLE/index.htm.

fluxes of objects in the images were used to correct for variable extinction. Determining the absolute photometry of the WIRCam image is not straightforward because there were no standard star observations. Our initial attempt was to calibrate the WIRCam image using 2MASS objects, but this was not successful. We found that objects with sufficient signal-to-noise ratios (S/Ns) in the 2MASS catalog are in the nonlinear regime of WIRCam. On the other hand, objects in the WIRCam linear regime are close to the detection limits of 2MASS where selection effects bias the 2MASS magnitudes. These make the calibration not better than 5%. Thus, we decided not to rely on 2MASS and instead calibrated the WIRCam image using our MOIRCS image (see § 2.2.2), which was calibrated with frequent standard star observations.

The final WIRCam K_s-band mosaic covers an area of $30' \times 30'$. Approximately 550 arcmin^2 has at least 10 hr of integration, and the deepest area has 39.7 hr of integration. The image FWHM is $\sim 0.8''$ and is quite uniform across the field. The rms astrometry error between the WIRCam catalog and the ACS/SuprimeCam reference catalog is $0.13''$. The typical 5 σ limiting magnitude in the 550 arcmin^2 deep area is $K_{s,\,AB} = 24.8$.

2.2.2. MOIRCS Imaging

MOIRCS contains two 2k × 2k HAWAII2 detectors covering a field of view of $\sim 4' \times 7'$ with a $0.117''$ pixel scale. Our group and Japanese groups led by various investigators have imaged the ACS and *Spitzer* GOODS-N regions with multiple pointings in the K_s band. Part of the Japanese data was published in Kajisawa et al. (2006). Here we include all our data, taken between 2005 December and 2008 January, and all the data available in the Subaru archive, taken between 2005 January and 2006 May. The majority of the observations were performed under photometric conditions with excellent seeing of $0.25''-0.6''$. A very small fraction of the data has large extinctions of >0.5 mag or poor seeing of $>0.7''$, and these observations were excluded in this work.

The reduction of the MOIRCS images also used the SIMPLE package and is almost identical to the reduction of the WIRCam images described above. Here we only describe the differences. MOIRCS produces nearly circular fringes in roughly half of the images in K_s. The fringes were modeled in polar coordinates where they are almost straight lines and were subtracted from the images in the original Cartesian coordinates. The MOIRCS images were calibrated by observing various UKIRT Faint Standards (Hawarden et al. 2001) at least every half night on each detector. K_s band magnitudes of the standard stars were estimated by interpolating the H and K magnitudes in the UKIRT list assuming a power-law SED and using the H and K passbands for the UKIRT broadband filters and the MOIRCS K_s passband (see Tokunaga et al. 2002). Data taken under nonphotometric conditions and poorly calibrated archive data were recalibrated with photometric data taken by our group.

The final MOIRCS K_s mosaic contains more than 20 pointings with different centers and position angles. The final mosaic has a total area of approximately 250 arcmin^2. For the region covered by the MOIRCS mosaic, the median 5 σ limit is $K_{s,\,AB} = 24.85$, comparable to that of the WIRCam image. However, because of the different strategies adopted by the various groups, the MOIRCS coverage is extremely nonuniform. The deepest MOIRCS area is around the Hubble Deep Field–North (HDF-N) proper with a total integration time of ~ 22 hr and extremely deep 5 σ limits of $K_{s,\,AB} = 26.2-26.7$. At some edges of the ACS and *Spitzer* GOODS-N regions the integration times are less than 20 minutes and the limiting magnitudes become <23.9. The MOIRCS mosaic has a very high image quality of $0.4''-0.5''$ over the entire field of view. The rms astrometry error be-

tween the MOIRCS positions and the ACS/SuprimeCam reference catalog is $0.08''$.

2.2.3. K_s Catalog

We defined a sample of 6909 sources within the most uniformly covered ACS GOODS-N region (145 arcmin^2) having $K_{s,\,AB} < 24.5$ in the WIRCam image, where $K_{s,\,AB}$ is a $3''$ diameter aperture magnitude corrected to a $6''$ diameter magnitude using a median offset measured for the brighter objects.

We list these sources in Table 1 ordered by K_s magnitude. We also give the flux and error from the WIRCAM image measured with the AUTO magnitude of SExtractor, which may provide a better approximation to the total magnitude for brighter galaxies in the sample. In constructing the catalog we eliminated a number of sources that lay within $3''$ of a brighter object and where reliable photometry and spectroscopy could not be obtained. We also excluded objects that lay within an $8''$ radius of the nine brightest stars in the field for the same reason. We eliminated artifacts and fragments of larger galaxies by visual inspection of the images and by cross-comparing the independent MOIRCS and WIRCam data. In the table we give the catalog number (col. [1]), the right ascension and declination (cols. [2]–[3]), the flux and 1 σ error in μJy corresponding to the SExtractor AUTO magnitude (cols. [4]–[5]), the K_s magnitude (col. [6]), the SExtractor AUTO magnitudes measured in the four ACS bands (cols. [7]–[10]), and the ground-based U-band magnitudes measured in a $3''$ diameter aperture and corrected to a $6''$ diameter magnitude using a median offset (col. [11]). We describe the remaining five columns of Table 1 in § 3.

2.3. Mid-Infrared Imaging

We took as our primary MIR sample the DR1+ Multi-Band Imaging Photometer for *Spitzer* (MIPS; Rieke et al. 2004) 24 μm source list of 1199 sources with fluxes above 80 μJy measured from the version 0.36 MIPS 24 μm map of the *Spitzer* Legacy Program. This source list is a subset of a more extensive catalog that will be presented by R.-R. Chary et al. (2008, in preparation). The positions of corresponding *Spitzer* Infrared Array Camera (IRAC; Fazio et al. 2004) sources were used to measure the 24 μm fluxes, where possible. We give this sample ordered by 24 μm flux in Table 2. Assigning NIR and optical counterparts to the 24 μm sources is complicated because of the uncertainties in the positions. We first applied the uniform offset of $-0.4''$ in declination to bring the absolute astrometry into the VLA frame. We next checked the relative astrometry by measuring the positions of the 24 μm sources on the K_s images in cases in which there was an unambiguous K_s counterpart. There appears to be a slight distortion in the 24 μm astrometry relative to both the K_s image and the 20 cm image, but the effect is not large ($\lesssim 0.5''$ over the entire image). We used a linear fit to remove this. We then measured the position of the nearest K_s source. In most cases the counterpart is unambiguous; all but 65 of the sources have a K_s counterpart within $1''$. This reflects the use of the IRAC source positions as priors in generating the 24 μm catalog. However, in some cases the 24 μm source lies between two NIR galaxies, likely as a consequence of blending. In these cases we assigned the source to the nearest galaxy, or, in the most ambiguous cases, to the brightest nearby galaxy using the IRAC images, where available, or the K_s image otherwise. We give the initial position of each 24 μm source (after astrometric correction) in columns (1) and (2) of Table 2, and we give the position of the adopted counterpart in columns (3) and (4). The 14 sources with separations greater than $1.5''$ from the counterpart are marked with the letter "w" after column (11). These counterparts should be treated with caution. The associated

TABLE 1
ACS GOODS-N Region $K_{s,\,AB} < 24.5$ Sample

Number (1)	R.A. (J2000.0) (2)	Decl. (J2000.0) (3)	Flux (4)	Error (5)	K_s (6)	F850LP (7)	F775W (8)	F606W (9)	F435W (10)	U (11)	$z_{\rm spec}$ (12)	Source (13)	$f_{24\,\mu m}$ (μJy) (14)	$L_{2-8\,\rm keV}$ (10^{40} ergs s^{-1}) (15)	$L_{0.5-2\,\rm keV}$ (10^{40} ergs s^{-1}) (16)
1.........................	189.377319	62.29675	1905.8	0.17	15.59	15.95	16.85	17.38	18.03	18.04	Star	1	...	...	...
2.........................	189.394943	62.24295	1893.3	0.18	15.61	16.16	16.86	17.60	18.48	19.20	Star	3	...	...	...
3.........................	189.105804	62.23464	1311.5	0.17	15.99	16.73	17.44	18.75	20.46	21.82	Star	3 5	...	...	...
4.........................	189.318695	62.28870	1145.1	0.17	16.13	16.93	17.62	19.00	20.73	22.14	Star	1	...	...	...
5.........................	189.241913	62.29114	955.51	0.16	16.32	16.55	16.99	17.80	18.39	17.71	Star	1	...	...	...
6.........................	189.069931	62.26203	925.89	0.16	16.36	17.20	17.93	19.39	21.25	22.58	Star	3	...	...	...
7.........................	189.436905	62.25447	904.58	0.16	16.39	16.51	17.04	17.73	18.57	17.92	Star	1	...	...	...
8.........................	189.331253	62.21222	858.91	0.16	16.44	16.97	17.39	18.20	19.27	20.62	Star	1 3 5	...	...	...
9.........................	189.406876	62.29158	866.33	0.15	16.44	16.44	16.87	17.60	17.93	17.45	Star	1	...	...	...
10.........................	189.171738	62.12906	850.35	0.16	16.45	16.71	17.02	18.05	18.73	18.86	Star	3	...	...	...
11.........................	189.324051	62.36736	591.90	0.18	16.89	17.43	18.22	19.76	21.68	22.90	Star	1	...	...	...
12.........................	189.243301	62.15983	558.92	0.16	16.90	16.89	17.11	17.89	18.44	18.26	Star	1 5	...	...	...
13.........................	189.059051	62.22419	539.65	0.17	16.95	17.42	18.10	19.32	21.04	22.32	Star	3	...	...	...
14.........................	189.195038	62.27681	490.52	0.17	17.06	17.42	18.02	18.84	20.22	21.64	Star	1 5	...	...	...
15.........................	189.315536	62.33242	480.08	0.15	17.07	17.57	18.49	19.86	21.77	22.98	Star	1	...	...	...
16.........................	189.484085	62.25370	611.27	0.30	17.09	17.90	18.15	18.74	20.29	20.94	0.1901	1 3 7	...	...	...
17.........................	189.316330	62.19973	543.37	0.25	17.29	17.78	18.08	18.71	20.07	21.11	0.1063	1 3	221	...	0.17
18.........................	189.287079	62.29700	385.62	0.16	17.30	17.02	17.31	18.09	18.68	17.70	Star	3	...	...	...
19.........................	189.481995	62.25178	830.05	0.26	17.34	18.14	18.50	19.28	20.90	22.35	0.1890	2 3	683	...	...
20.........................	189.243088	62.16611	652.10	0.32	17.38	17.54	17.74	18.23	19.20	20.39	0.1363	1 3 5 7	518	...	0.38
21.........................	189.304703	62.26983	359.44	0.16	17.39	17.48	17.85	18.61	19.31	20.26	Star	1	...	...	...
22.........................	189.205917	62.22967	410.38	0.23	17.41	17.99	18.26	18.83	20.14	20.91	0.0893	2 3 5	...	...	0.09
23.........................	189.046081	62.14755	316.06	0.14	17.51	17.72	18.23	18.97	20.00	21.34	Star	1	...	...	...
24.........................	189.429108	62.30836	310.04	0.15	17.52	18.10	18.86	20.84	22.98	24.40	Star	1	...	...	...
25.........................	189.124496	62.29128	310.71	0.15	17.54	17.98	18.40	19.55	21.42	22.87	Star	1 3	...	...	...
26.........................	189.356873	62.28011	307.88	0.15	17.54	18.08	18.68	20.33	22.24	23.49	Star	3	...	...	...
27.........................	189.515167	62.28647	408.17	0.24	17.56	18.82	19.15	19.83	21.15	21.99	0.2790	1 3	1430	...	...
28.........................	189.143616	62.20361	391.80	0.25	17.58	18.79	19.15	19.95	21.45	22.27	0.4575	2 3 5	1290	20.3	18.5
29.........................	189.373825	62.32628	448.78	0.22	17.59	18.61	18.95	19.84	21.75	22.97	0.3177	1 2	...	...	...
30.........................	189.369370	62.30920	285.35	0.15	17.64	18.13	18.70	20.22	22.17	23.65	Star	3	...	...	...

Note.—Table 1 is published in its entirety in the electronic edition of the *Astrophysical Journal*. A portion is shown here for guidance regarding its form and content.

TABLE 2
Spitzer GOODS-N REGION 24 μm SAMPLE

R.A. (J2000.0) (1)	Decl. (J2000.0) (2)	R.A. (J2000.0) (3)	Decl. (J2000.0) (4)	$f_{24\,\mu m}$ (μJy) (5)	K_s (6)	F850LP (7)	F775W (8)	F606W (9)	F435W (10)	U (11)	z_{spec} (12)	Source (13)	$L_{2-8\,keV}$ (10^{40} ergs s^{-1}) (14)	$L_{0.5-2\,keV}$ (10^{40} ergs s^{-1}) (15)	$f_{20\,cm}$ (μJy) (16)
189.503754	62.22667	189.503876	62.22667	4290	17.28	18.41	18.72	. . .	19.11	18.59	0.4430	3	3019.	3051	190
189.125214	62.09511	189.124863	62.09505	2460	18.86	20.24	20.53	21.35	25.76	22.64	0.4832	1 3	504.1	. . .	82
189.033844	62.17664	189.033783	62.17661	2300	19.35	20.59	20.98	22.24	23.79	23.83	0.6790	2 3 7	318.0	24.2	217
189.469635	62.27450	189.469711	62.27450	1720	17.70	18.61	18.94	19.46	20.03	19.23	0.3060	2 3	1353.	797.	79
189.622528	62.28028	189.622498	62.28042	1660	17.64	18.71	18.98	. . .	20.49	20.51	0.2777	1 3	. . .	. . .	. . .
189.204666	62.07744	189.204224	62.07747	1540	15.42	16.23	17.09	. . .	18.61	19.30	0.1130	3	. . .	2.2	850
189.148239	62.24006	189.148239	62.24000	1480	20.34	22.90	23.27	23.75	24.06	23.57	2.0050	3 8	5510.	459.	87
188.998795	62.26389	188.998871	62.26386	1470	17.88	18.62	18.94	19.45	24.02	21.00	0.3750	3	. . .	7.5	212
189.207001	62.12728	189.206909	62.12725	1450	21.19	22.87	23.21	23.64	23.89	23.70	1.6095	1 3	30340	6040	307
189.515091	62.28647	189.515167	62.28650	1430	17.56	18.82	19.15	19.83	21.15	21.99	0.2790	1 3	. . .	. . .	253
189.143600	62.20364	189.143661	62.20359	1290	17.57	18.79	19.15	19.95	21.45	22.20	0.4575	1 2 3 5	20.7	18.9	233
189.051635	62.19453	189.051940	62.19458	1240	18.05	18.96	19.24	19.86	21.09	21.45	0.2760	1 2 3	. . .	. . .	174
189.319382	62.29261	189.319412	62.29264	1230	20.16	22.11	22.68	23.63	24.79	24.75	1.1460	3	11042	2719	346
189.000534	62.17981	189.000717	62.17978	1220	22.10	24.32	24.63	25.08	25.58	24.18	2.0020	8	. . .	. . .	131
189.013488	62.18639	189.013534	62.18636	1210	18.53	20.00	20.30	21.22	22.38	22.37	0.6380	2 3 7	. . .	23.9	124
189.290573	62.14475	189.290619	62.14481	1120	19.34	21.40	21.91	. . .	24.19	23.94	0.9020	3	. . .	38.0	. . .
189.392761	62.15473	189.392853	62.15878	1110	17.40	18.65	19.01	. . .	20.82	21.27	0.1890	3	. . .	2.4	142
189.228271	62.07419	189.228210	62.07411	1040	17.87	18.92	19.26	. . .	21.17	21.35	0.2870	3	. . .	10.8	60
189.590714	62.28514	189.590683	62.28528	1030	20.20	21.34	21.90	. . .	23.47	23.43	1.5960 :	1	. . .	. . .	. . .
189.356552	62.32817	189.356339	62.32814	1000	17.96	18.13	18.32	18.73	19.66	20.68	0.2780	2 3	. . .	2.1	122
189.426178	62.25508	189.426178	62.25508	992	18.18	18.44	18.57	18.96	19.70	20.42	0.0700	2 3 7	1.4	0.3	. . .
189.212997	62.17525	189.212997	62.17522	984	18.54	19.93	20.36	21.17	22.71	23.25	0.4100	2 3 5 6	. . .	5.6	95
189.194458	62.14256	189.194458	62.14258	982	19.15	20.65	21.18	22.13	22.85	22.94	0.9710	2 3 7	. . .	21.3	80
189.081161	62.21464	189.081115	62.21461	976	18.66	19.72	20.06	20.93	22.36	23.15	0.4734	2 3 5	. . .	6.7	108
189.338242	62.21308	189.338684	62.21311	966	18.03	17.48	17.65	18.13	18.92	20.74	0.1060	2 3 5	. . .	. . .	. . .
189.360474	62.34072	189.360413	62.34069	932	21.24	23.58	24.07	24.71	25.92	26.16	2.3650	1	4325.	498.	102
188.991425	62.26025	188.991425	62.26022	925	17.92	19.25	19.74	. . .	22.08	22.45	0.3760	3	. . .	. . .	209
189.278549	62.28392	189.278625	62.28392	903	19.00	19.86	19.88	19.84	20.08	19.36	1.0190	1 3 4	10153	8434	. . .
189.460556	62.19550	189.460327	62.19536	889	17.17	18.51	18.90	. . .	20.90	21.46	0.1890	3	. . .	1.2	198
189.365570	62.17667	189.365387	62.17667	871	17.40	17.70	17.92	18.48	22.72	20.93	0.2140	3	. . .	1.3	. . .

NOTE.—Table 2 is published in its entirety in the electronic edition of the *Astrophysical Journal*. A portion is shown here for guidance regarding its form and content.

24 μm fluxes may be overestimated if the offset is a consequence of blending. We also list in Table 2 the 24 μm flux (col. [5]), the K_s magnitude (col. [6]), and the four ACS magnitudes (cols. [7]–[10]). Where the object lies off the *HST* image, we give the z', I, and B ground-based magnitudes instead (Capak et al. 2004). In these cases the F606W column is left blank. We give the U-band magnitude in column (11). We describe the remaining five columns of Table 2 in § 3.

2.4. *Near-Ultraviolet and Far-Ultraviolet Imaging*

The *Galaxy Evolution Explorer* (*GALEX*) mission (Martin et al. 2005) obtained a deep 150 ks exposure of the ACS GOODS-N region in early 2004. We measured the near-ultraviolet (NUV; 2371 Å central wavelength) and far-ultraviolet (FUV; 1528 Å central wavelength) magnitudes from these images, which we obtained from the Multimission Archive at STScI (MAST). We used as a prior the positions of the F435W$_{AB}$ = 26 galaxy sample. Given the large point-spread function (4.5″–6″ FWHM) of *GALEX*, we used an 8″ diameter aperture to measure the magnitudes using the *GALEX* zeropoints of 20.08 for the NUV image and 18.82 for the FUV image. For the brighter objects (F435W$_{AB}$ = 20–23.5 mag) we measured the median offset between the 8″ magnitudes and the magnitudes that we measured in a 24″ diameter aperture. We then used this to correct all of the 8″ magnitudes to approximate total magnitudes. The magnitudes agree on average to within 0.05 mag with the SExtractor based magnitudes given in the *GALEX* NUV+ FUV merged catalog for the region. We measured the noise level by randomly positioning apertures on blank areas of the sky and measuring the dispersion. We found 1 σ limits of 26.8 for the NUV image and 27.4 for the FUV image.

GALEX has a large point-spread function, so contamination by neighbors is a serious problem. Thus, in generating an NUV+ FUV sample of isolated galaxies, we eliminated sources that were closer than 8″ to a brighter *GALEX* source at the same wavelength or where, based on a visual inspection, the position was clearly contaminated by the wings of a nearby bright source. A substantial fraction of the galaxies in the optical sample are eliminated by this isolation requirement. The final sample contains 1016 sources with NUV$_{AB}$ < 25 and 478 sources with FUV$_{AB}$ < 25.5 (with considerable overlap between the two). We list these sources in Table 3 ordered by NUV magnitude. We give the right ascension and declination (cols. [1] and [2]), the NUV magnitude (col. [3]), and the FUV magnitude (col. [4]). Where we find a negative flux in the aperture, we show the magnitude corresponding to the absolute flux with a minus sign in front. We also give the 24 μm flux (col. [5]), the K_s magnitude (col. [6]), the four ACS magnitudes (cols. [7]–[10]), and the U-band magnitude (col. [11]). We describe the remaining five columns of Table 3 in § 3.

2.5. *X-Ray and Radio Imaging*

Richards (2000) presented a catalog of 20 cm sources detected in the VLA map of the HDF-N, which covers a 40′ diameter region with an effective resolution of 1.8″. The absolute radio positions are known to 0.1″–0.2″ rms. We cross-identified our catalogs with the radio catalog to obtain 20 cm fluxes.

Alexander et al. (2003) presented the 2 Ms X-ray image of the *Chandra* Deep Field–North (CDF-N), which they aligned with the Richards (2000) VLA image. Near the aim point the X-ray data reach limiting fluxes of $f_{2-8\,keV} \approx 1.4 \times 10^{-16}$ ergs cm^{-2} s^{-1} and $f_{0.5-2\,keV} \approx 1.5 \times 10^{-17}$ ergs cm^{-2} s^{-1}. We use these data to identify AGNs, which we define on energetic grounds as any source more luminous than 10^{42} ergs s^{-1} (Zezas et al. 1998; Moran et al. 1999) calculated in either the rest-frame 0.5–2 keV (soft) or rest-frame 2–8 keV (hard) band. Trouille et al. (2008) present a table

of redshifts for the full X-ray sample, including sources that lie outside the ACS or *Spitzer* GOODS-N regions.

3. THE SPECTROSCOPIC DATA

Our primary goal for this paper was to obtain the most complete and homogeneous spectral database possible for the GOODS-N field. Over the years a number of groups have made observations of this region, first primarily using the Low-Resolution Imaging Spectrograph (LRIS; Oke et al. 1995) on the Keck I 10 m telescope (these data are summarized in Cohen et al. 2000) and later using the large-format Deep Extragalactic Imaging Multi-Object Spectrograph (DEIMOS; Faber et al. 2003) on the Keck II 10 m telescope. Wirth et al. (2004; Team Keck Treasury Redshift Survey [TKRS]) and Cowie et al. (2004) presented large samples of magnitude-selected redshifts obtained using DEIMOS. In addition, Reddy et al. (2006) gave a substantial sample of color-selected redshifts, Chapman et al. (2004, 2005) and Swinbank et al. (2004) presented a small number of radio/submillimeter redshifts, and Treu et al. (2005) measured redshifts for a sample of spheroids. Barger et al. (2003), Trouille et al. (2008), and Barger et al. (2007) carried out extensive observations of the X-ray and 20 cm sources in the CDF-N.

Here we have added to these samples by observing all of the missing or unidentified galaxies in the F435W, F850LP, K_s, and 24 μm selected samples. In order to provide a uniform spectral database, we also reobserved sources where the original spectra were of poor quality or where previous redshifts were obtained with instruments other than DEIMOS, as well as where the existing redshift identifications were unconvincing (a small number).

We made our observations over a number of DEIMOS runs between 2004 and 2007. We used the 600 line mm^{-1} grating, giving a resolution of 3.5 Å and a wavelength coverage of 5300 Å, which was also the configuration used in the TKRS observations. The spectra were centered at an average wavelength of 7200 Å, although the exact wavelength range for each spectrum depends on the slit position. Each ∼1 hr exposure was broken into three subsets, with the objects stepped along the slit by 1.5″ in each direction. Unidentified sources were continuously reobserved giving maximum exposure times of up to 7 hr. The spectra were reduced in the same way as previous LRIS spectra (Cowie et al. 1996). Only spectra that could be confidently identified based on multiple emission and/or absorption lines were included in the sample. A number of spectra were identified based on the doublet structure of the [O II] 3727 Å line, which is resolved in the spectra.

In Table 4 we list the redshifts for 2907 sources in the ACS GOODS-N field. Only sources with $K_{s,\,AB}$ < 24.5 or F850LP$_{AB}$ < 26 are included, which omits a small number of emission-line galaxies with known redshifts in the area. (A table of emission-line galaxies will be given in E. M. Hu et al. 2008, in preparation.) The table is ordered by right ascension. We give the right ascension and declination (cols. [1] and [2]), the K_s, F850LP, F775W, F606W, F435W, and U magnitudes (cols. [3]–[8]), the spectroscopic redshift (col. [9]), the source of the redshift (col. [10]; see Table 6), the 24 μm flux in μJy (col. [11]), and the rest-frame 2–8 keV (col. [12]) and 0.5–2 keV (col. [13]) X-ray luminosities in units of 10^{40} ergs s^{-1}. Four stars were classified primarily on compactness and on their unambiguous stellar colors. These are shown without a source number in the tables and may be removed if desired.

We summarize the fraction of spectroscopically identified objects as a function of color and magnitude in Table 5. The redshift identifications are greater than 90% complete to magnitudes of F435W$_{AB}$ = 24.5, F850LP$_{AB}$ = 23.3, and $K_{s,\,AB}$ = 21.5.

In Table 6 we list the published catalogs (the references are given in col. [5]) that we used in assembling our various redshift

<div align="center">

TABLE 3

ACS GOODS-N Region NUV+FUV Sample

</div>

R.A. (J2000.0) (1)	Decl. (J2000.0) (2)	NUV (3)	FUV (4)	$f_{24\,\mu m}$ (μJy) (5)	K_s (6)	F850LP (7)	F775W (8)	F606W (9)	F435W (10)	U (11)	$z_{\rm spec}$ (12)	Source (13)	$L_{2-8\,{\rm keV}}$ (10^{40} ergs s^{-1}) (14)	$L_{0.5-2\,{\rm keV}}$ (10^{40} ergs s^{-1}) (15)	$f_{20\,{\rm cm}}$ (μJy) (16)
189.278625	62.28391	19.89	20.65	903	19.24	19.86	19.88	19.84	20.08	19.36	1.0190	1 3 4	10032	8334	. . .
189.153595	62.19299	20.06	20.37	732	17.75	17.98	18.06	18.36	18.86	19.94	0.0790	2 3 5	. . .	0.0	. . .
189.287094	62.29699	20.30	26.87	. . .	17.46	17.02	17.31	18.09	18.68	17.70	star	3	. . .	. . .	. . .
189.356339	62.32814	20.49	21.25	1000	17.47	18.13	18.32	18.73	19.66	20.65	0.2780	2 3	. . .	2.4	. . .
189.338516	62.21310	20.70	21.18	966	16.75	17.48	17.65	18.13	18.92	20.80	0.1060	2 3 5	. . .	0.2	. . .
189.201248	62.24068	20.78	21.15	460	18.58	18.93	19.00	19.32	19.89	20.17	0.1390	2 3 4 5	. . .	0.4	. . .
189.243088	62.16612	20.82	21.23	518	16.95	17.54	17.74	18.23	19.20	20.39	0.1363	1 3 5 7	. . .	0.3	. . .
189.469711	62.27448	20.95	21.36	1720	17.71	18.61	18.94	19.46	20.03	19.26	0.3060	2 3	1381.	813.	. . .
189.103424	62.12196	20.99	21.46	308	18.58	18.80	18.89	19.25	19.85	20.30	0.1140	2 3	. . .	. . .	. . .
189.166962	62.14449	21.19	21.57	327	18.00	18.36	18.52	18.96	19.72	20.42	0.0872	2 3	. . .	. . .	. . .
189.173462	62.19215	21.22	21.42	. . .	19.74	19.74	19.77	20.03	20.45	21.02	0.0892	1 2 5	. . .	0.2	. . .
189.256317	62.31183	21.24	21.90	377	17.35	18.15	18.40	18.94	20.13	21.49	0.2330	1 3	. . .	2.3	. . .
189.189240	62.20376	21.29	23.83	. . .	22.66	21.20	20.98	20.79	20.71	20.21	star	3 5	. . .	. . .	. . .
189.000701	62.23579	21.35	21.80	330	18.23	18.64	18.78	19.21	19.95	20.58	0.1140	1 2	. . .	. . .	. . .
189.258499	62.18968	21.37	21.70	191	18.54	18.87	19.01	19.41	20.16	21.06	0.1360	2 3 5 6 7	. . .	0.2	. . .
189.275757	62.28677	21.46	22.14	596	17.48	18.25	18.48	19.04	20.23	21.34	0.2540	2 3	5.9	0.9	. . .
189.389099	62.22782	21.53	21.87	139	18.71	18.95	19.07	19.47	20.21	20.92	0.1050	1 2 7	. . .	. . .	. . .
189.151459	62.11858	21.60	22.35	296	18.82	19.47	19.66	20.04	20.89	21.30	0.2760	2 3	. . .	. . .	. . .
189.212723	62.22241	21.61	22.11	. . .	19.30	19.56	19.64	19.94	20.79	21.41	0.2008	2 3 5	. . .	. . .	. . .
189.241898	62.29115	21.63	26.71	. . .	16.51	16.55	16.99	17.80	18.39	17.71	star	1	. . .	. . .	. . .
189.261353	62.26208	21.67	22.94	473	18.51	19.40	19.70	20.39	21.03	21.22	0.5120	2 3 5 7	2914.	686.	. . .
189.406876	62.29157	21.68	−27.62	. . .	16.59	16.44	16.87	17.60	17.93	17.45	star	1	. . .	. . .	. . .
189.052002	62.19455	21.70	22.59	1240	18.04	18.96	19.24	19.86	21.09	21.48	0.2760	1 2 3	. . .	. . .	. . .
189.066177	62.21037	21.71	22.53	396	18.74	19.25	19.47	19.93	20.92	21.41	0.2857	1 5	. . .	. . .	. . .
189.426239	62.25509	21.75	22.54	992	18.15	18.44	18.57	18.96	19.70	20.41	0.0700	2 3 7	1.5	0.4	. . .
189.399048	62.30290	21.76	22.23	. . .	20.81	20.70	20.81	21.11	22.12	22.20	0.2990	2 3	. . .	. . .	. . .
189.299118	62.25406	21.79	22.38	88	19.79	19.97	20.13	20.42	21.30	21.69	0.2990	2 5	. . .	. . .	. . .
189.135498	62.28315	21.80	23.32	735	17.82	18.60	18.90	19.54	20.64	21.92	0.4370	2 3	. . .	. . .	. . .
188.953766	62.19576	21.92	22.25	. . .	21.98	19.81	19.88	20.21	20.77	21.91	0.1192	2	. . .	. . .	. . .
188.948349	62.20189	21.98	22.46	. . .	19.72	19.81	19.91	20.21	20.78	21.26	0.0787	2 3	. . .	. . .	. . .

Note.—Table 3 is published in its entirety in the electronic edition of the *Astrophysical Journal*. A portion is shown here for guidance regarding its form and content.

TABLE 4
ACS GOODS-N Region Spectroscopic Redshifts

R.A. (J2000.0) (1)	Decl. (J2000.0) (2)	K_s (3)	F850LP (4)	F775W (5)	F606W (6)	F435W (7)	U (8)	z_{spec} (9)	Source (10)	$f_{24\,\mu m}$ (μJy) (11)	$L_{2-8\,keV}$ (10^{40} ergs s^{-1}) (12)	$L_{0.5-2\,keV}$ (10^{40} ergs s^{-1}) (13)
188.922012	62.19910	22.63	23.17	23.41	23.64	23.71	23.32	1.5367	1	...	...	...
188.923355	62.19751	22.89	23.05	23.00	23.26	23.22	22.72	1.1073	2	...	...	...
188.925476	62.19721	23.62	24.04	24.27	24.53	24.45	24.15	1.1410	1	...	...	...
188.927078	62.19710	22.50	23.23	23.75	24.31	24.71	24.42	1.1452	1	...	...	...
188.930313	62.19232	22.36	22.58	22.72	23.24	23.90	24.11	0.5583	2	...	...	...
188.931183	62.20426	22.56	22.80	22.97	23.41	24.49	24.42	0.3269	1	...	...	...
188.933411	62.19930	20.96	22.71	23.44	24.32	24.84	25.02	1.3151	1	...	...	...
188.934525	62.20675	20.47	22.55	23.51	24.96	25.89	27.11	1.3140	1	...	...	...
188.938339	62.20606	20.59	21.38	21.63	22.31	23.39	23.67	0.4734	2	...	...	...
188.939072	62.21012	22.68	23.02	23.20	24.03	24.57	24.68	0.7133	2	...	...	...
188.939331	62.19835	21.44	22.81	23.53	25.18	26.54	24.33	0.9599	1	...	...	...
188.939713	62.19888	20.26	21.45	21.99	22.98	23.72	23.67	0.9590	1	225	...	...
188.940292	62.19432	20.73	21.10	21.25	21.69	22.37	22.14	0.4733	1 2	...	...	...
188.941605	62.20118	18.76	20.15	20.72	22.30	24.44	25.44	0.7968	1	...	...	...
188.941803	62.19801	21.37	21.71	21.94	22.26	23.08	22.88	0.2976	1	...	...	...
188.943405	62.20610	22.86	23.57	24.10	24.52	24.72	24.75	1.3371	1	...	...	...
188.943649	62.20052	21.66	21.72	21.86	22.43	23.61	25.10	star	2	...	...	...
188.948349	62.20189	19.72	19.81	19.91	20.21	20.78	21.26	0.0787	2 3	...	...	...
188.949982	62.21469	23.97	24.56	24.50	24.49	24.55	23.60	1.7980	4	...	...	...
188.950317	62.20343	21.39	21.56	21.65	22.14	22.84	22.84	0.5084	2	...	...	...
188.951263	62.18684	21.82	22.15	22.28	22.78	23.31	23.47	0.5065	2	...	...	...
188.951614	62.18248	19.60	20.41	20.65	21.15	22.26	22.34	0.3000	1	86	...	...
188.952530	62.19215	19.54	20.66	21.17	22.67	24.44	24.61	0.8429	2 7	...	...	...
188.952576	62.19814	22.36	22.55	22.86	23.52	23.77	23.57	1.0007	1 2	...	...	...
188.953720	62.21213	22.58	23.28	23.44	23.96	25.05	24.88	0.4102	2	...	...	...
188.953766	62.19576	21.98	19.81	19.88	20.21	20.77	21.91	0.1192	2	...	...	...
188.954742	62.18175	22.65	23.30	23.45	24.09	25.00	25.61	0.5075	2	...	...	...
188.956726	62.21053	19.56	20.51	20.87	21.86	23.73	24.82	0.4573	1 7	...	...	...
188.958984	62.19461	22.62	23.40	23.83	23.95	23.99	23.63	1.3274	1	...	...	...
188.960098	62.18470	22.56	22.80	23.11	23.68	23.87	23.53	1.0872	1	...	...	...

Note.—Table 4 is published in its entirety in the electronic edition of the *Astrophysical Journal*. A portion is shown here for guidance regarding its form and content.

tables. We have assigned a unique source number (col. [1]) to each catalog. It is this source number that appears in column (10) of Table 4. We also summarize in Table 6 the number of redshifts present in each catalog (col. [2]) and the number of redshifts that appear only in that catalog ("unique"; col. [3]). We give a cumulative redshift count of all the identified galaxies in column (4). Galaxies from sources 1 and 2 have uniform DEIMOS spectra, while galaxies from source 3 have LRIS spectra. The galaxies from these three sources form our *spectral* database.

We show the redshift distribution in Figure 1. Most of the redshifts are at $z < 1.6$ (2362 sources) where the [O II] 3727 Å line still lies in the DEIMOS spectroscopic range, 327 lie between $z = 1.6$ and 3.5, mostly from the LRIS observations of Reddy et al. (2006), and there are relatively few objects (only 21) with spectroscopic redshifts $z > 3.5$. In total, 98 of the objects are classified as containing AGNs that could be significant contributors to the

galaxy light based on either their rest-frame hard or soft X-ray luminosities being above 10^{42} ergs s^{-1}. We show on the figure the redshift distribution for these AGNs (*red*).

We also list the spectroscopic redshifts for the $K_{s,\,AB} < 24.5$ sample as a function of K_s magnitude in Table 1 (col. [12]; there are redshifts for 2596 stars and galaxies in this sample), for the 24 μm sample as a function of 24 μm flux in Table 2 (col. [12]; the *Spitzer* area covered is larger than the area covered by the optical/NIR catalog, so 213 of the 743 galaxies and stars with spectroscopic identifications in this sample lie outside the ACS area), and for the NUV+FUV sample as a function of NUV magnitude in Table 3 (col. [12]).

The remaining columns in Table 1 are the source of the redshift (col. [13]), the 24 μm flux in μJy (col. [14]), and the rest-frame 2–8 keV (col. [15]) and 0.5–2 keV (col. [16]) luminosities in units of 10^{40} ergs s^{-1}. The remaining columns in Tables 2 and 3 are the source of the redshift (col. [13]), the rest-frame 2–8 keV (col. [14]) and 0.5–2 keV (col. [15]) luminosities in units of 10^{40} ergs s^{-1}, and the 20 cm flux in μJy (col. [16]).

In Figure 2 we show redshift versus 24 μm flux for the 80 μJy MIR sample. We use large red squares to denote AGNs with rest-frame hard or soft X-ray luminosities in excess of 10^{42} ergs s^{-1}. At the base of the plot we show a histogram of the fraction of sources per half-magnitude bin that remain spectroscopically unidentified. The sample is essentially complete to 500 μJy.

In Figure 3 we show redshift-magnitude diagrams for the (*a*) FUV$_{AB} < 25$, (*b*) NUV$_{AB} < 25$, and (*c*) $U_{AB} < 25$ samples.

TABLE 5
Spectroscopically Identified Fraction for the Optical and NIR Samples

Band	98%	95%	90%	80%
F435W	23.9	24.2	24.5	24.9
F606W	23.6	23.9	24.2	24.5
F775W	23.1	23.4	23.6	24.0
F850LP	22.6	22.9	23.3	23.7
K_s	20.7	21.0	21.5	22.2

TABLE 6
Source of Spectroscopic Redshifts

Source (1)	Number (2)	Unique[a] (3)	Cumulative (4)	Reference (5)
1........................	1506	842	1506	This work; see also Cowie et al. (2004)
2........................	1389	557	2551	TKRS; Wirth et al. (2004)
3........................	394	19	2581	Our LRIS spectra
4........................	343	224	2853	Reddy et al. (2006)
5........................	613	13	2879	Cohen et al. (2000); Cohen (2001)
6........................	114	1	2880	Lowenthal et al. (1997); Phillips et al. (1997)
7........................	243	2	2882	Treu et al. (2005)
8........................	14	8	2890	Chapman et al. (2004, 2005); Swinbank et al. (2004)
9........................	50	3	2893	Steidel et al. (2003)
10........................	44	5	2898	Dawson et al. (2001)
11........................	4	4	2902	Pope et al. (2008)
12........................	0	0	2902	Barger et al. (2003)[b]
13........................	2	0	2902	Daddi et al. (2008)
14........................	8	1	2903	MOIRCS spectra

[a] The number of sources for which only that catalog has obtained redshift identifications.

[b] We have not distinguished the observations made in the Barger et al. (2003) paper (literature source 12) from our DEIMOS and LRIS observations of the ACS GOODS-N area (literature sources 1 and 3), which is why zeros appear in the number and unique columns for Barger et al. (2003). However, we retain Barger et al. (2003) as a literature source in this table because it includes some ESI identifications that appear in the 24 μm catalog outside the ACS GOODS-N area.

In each panel we show the redshift at which the Lyman continuum break passes through the center of the filter (*dashed horizontal lines*; i.e., $z = 0.67$, $z = 1.6$, and $z = 3.06$, respectively, for the FUV, NUV, and *U*-band filters). The sharp cutoffs above these redshifts are clearly seen and, perhaps surprisingly, apply to both the AGNs (*large red squares*) and the galaxies, with very few sources in either category lying above the cutoffs. We return to this point when we consider LBG selection in § 4.1. In Figure 4 we show redshift-magnitude diagrams for the (*a*) F435W$_{AB}$ < 25, (*b*) F606W$_{AB}$ < 24, (*c*) F850LP$_{AB}$ < 24, and (*d*) $K_{s, AB}$ < 23 samples.

4. COLOR SELECTION TECHNIQUES

We use the spectroscopic sample to test three-color selection techniques that can be used to pick out galaxies in a given redshift range: the LBG dropout technique, the *BzK* color selection, and the H$^-$ method in the MIR. For each method there are two quantities of interest.

1. If one were to use the method to select galaxies in the given redshift range for spectroscopic follow-up or for direct analysis,

then the first quantity of interest is the fraction of objects that lie outside the redshift range that are found by the selection. We call this the selection contamination.

2. The second quantity of interest is the fraction of objects that lie in the redshift range that are actually found by the color selection. We call this the selection completeness.

In general, the color selections are tuned to provide a reasonable balance between selection contamination and selection completeness and can be adjusted to optimize one or the other. Thus, if one were using the color selection to choose objects for spectroscopic follow-up, a high level of contamination might be acceptable in order to make sure the sample contained most of the objects in the redshift range. On the other hand, if the primary goal were to choose a set of objects in the redshift range based on colors, then one might want to minimize contamination even if one missed a number of objects in the redshift range.

FIG. 1.—Redshift distribution of the sources in Table 4. The bin size is 0.01. AGNs are shown in red.
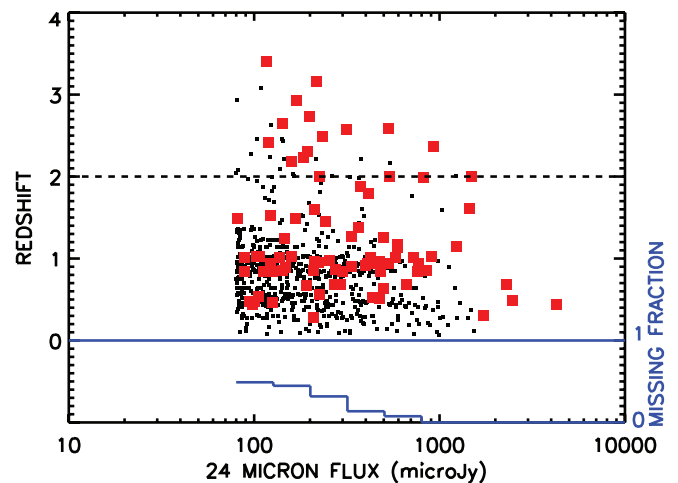
FIG. 2.—Redshift vs. 24 μm flux for the 80 μJy MIR sample. AGNs, defined as sources with rest-frame hard or soft X-ray luminosities >10^{42} ergs s^{-1}, are denoted by large red squares. The fraction of unidentified sources per 0.5 mag bin is shown in histogram form at the bottom of the plot (label is on right-hand *y*-axis). The dashed horizontal line shows $z = 2$.
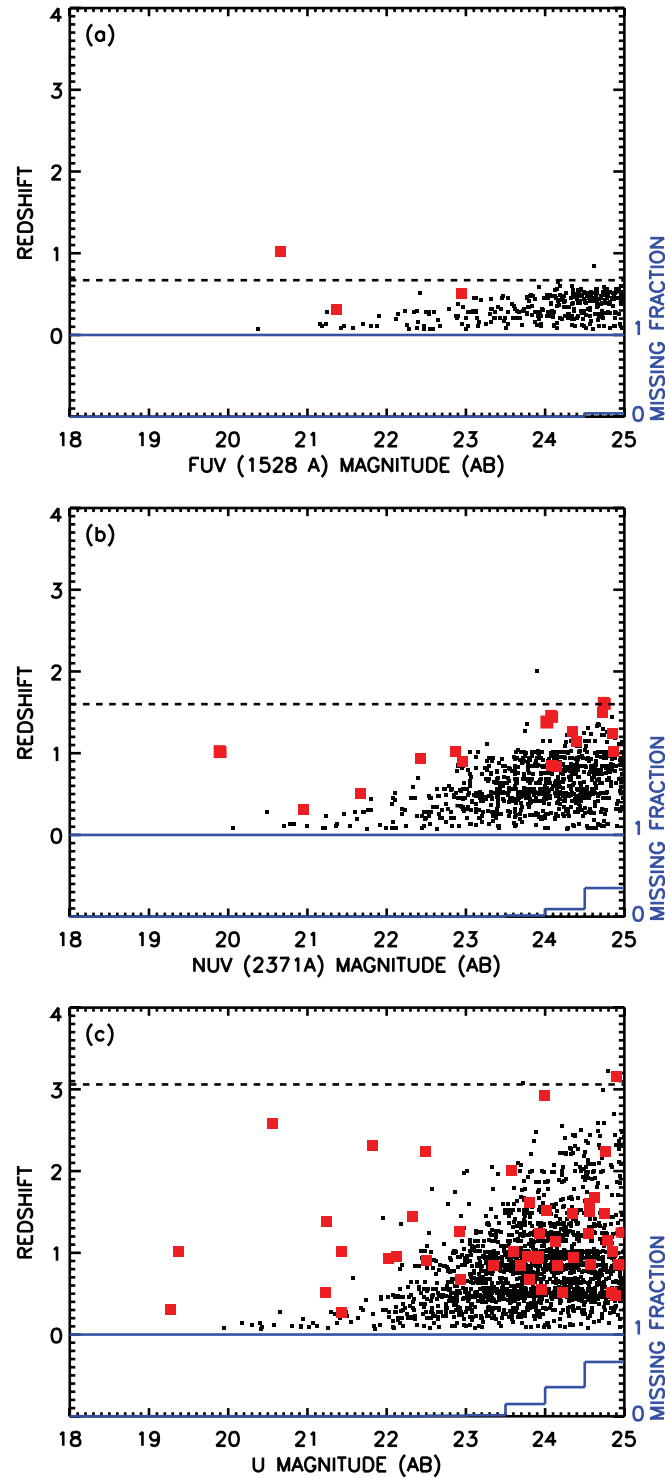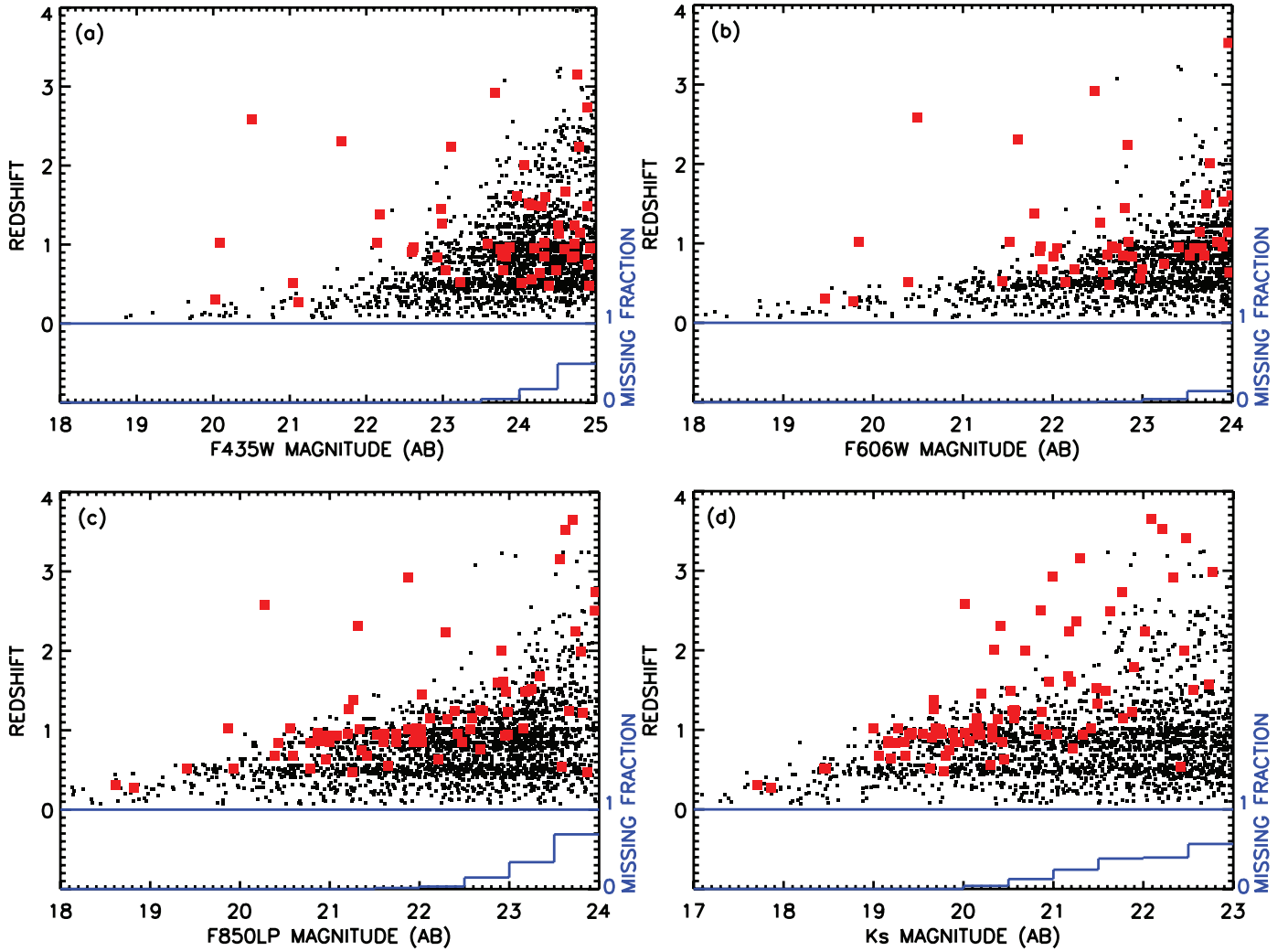
Fig. 3.—Redshift vs. (a) FUV_{AB} magnitude for the $FUV_{AB} < 25$ sample, (b) NUV_{AB} magnitude for the $NUV_{AB} < 25$ sample, and (c) U_{AB} magnitude for the $U_{AB} < 25$ sample. AGNs, defined as sources with rest-frame hard or soft X-ray luminosities $>10^{42}$ ergs s^{-1}, are denoted by large red squares. The dashed horizontal lines show the redshifts at which the Lyman continuum break passes through the center of each filter: (a) $z = 0.67$ for the FUV, (b) $z = 1.6$ for the NUV, and (c) $z = 3.06$ for the U-band. The fraction of unidentified sources per 0.5 mag bin is shown in histogram form at the bottom of each plot (label is on the right-hand y-axis).

4.1. The LBG Selection

In Figure 5 we show the $2.7 \leq z \leq 3.4$ LBG color-color selection (*blue solid lines*) for our 98.4% spectroscopically complete $F606W_{AB} < 23.5$ sample. This sample consists of 1197 galaxies and stars, only 18 of which are not identified. Our selection is

$$(U - F606W)_{AB} > 1.2 \qquad (1)$$

for $(F606W - F850LP)_{AB} \leq 0.25$, and

$$(U - F606W)_{AB} > (F606W - F850LP)_{AB} \times 2.4 + 0.6 \qquad (2)$$

for $0.25 < (F606W - F850LP)_{AB} < 0.8$.

Using the SExtractor stellarity index, as measured in the ACS F850LP image, we have divided the sample into extended (<0.5; Fig. 5a) and compact (>0.5; Fig. 5b) sources ($z \leq 2.7$ galaxies, *black diamonds*; $z > 2.7$ galaxies , *red inverted triangles*; spectroscopically identified stars, *purple stars*; unidentified sources, *green triangles*). We denote the AGNs (rest-frame hard or soft X-ray luminosities $>10^{42}$ ergs s^{-1}) with large squares (*blue for $z \leq 2.7$; red for $z > 2.7$*). We enclose in larger black squares those AGNs classified as broad-line AGNs, and we enclose in larger black diamonds those AGNs with high-excitation emission lines (C IV or [Ne V]).

The LBG selection works well for the one $z > 2.7$ galaxy (high selection completeness). This object is cleanly picked out at these magnitudes (Fig. 5a). In addition, only a small number of other sources cross the boundary in either Figures 5a or 5b (modest selection contamination). However, the three $z > 2.7$ AGNs are not picked out by the LBG selection, although they do lie close to the boundary. This is reasonable for the two compact $z > 2.7$ AGNs in Figure 5b. Both show AGN signatures in their optical spectra, and the dominant AGN light would not be expected to have a strong Lyman break. However, the $z > 2.7$ AGN in Figure 5a shows no AGN signatures in its optical spectrum, and it is dominated by the extended galaxy light. It would not be classified as an AGN based on its optical spectrum, which shows strong UV absorption lines and very weak Lyα emission. It appears that the AGN is weakening the break signature and dropping the object from the LBG selection while not dominating the longer wavelength light.

We show the break selection in a different way in Figure 6, where we plot a U-break parameter versus redshift in three magnitude intervals for every $F850LP_{AB} \geq 19$ source with a measured spectroscopic redshift. We define the U break parameter to be

$$(U - F606W)_{AB} - (F606W - F850LP)_{AB} \times 2.4 - 0.6. \qquad (3)$$

This is just a measure of how far above or below the diagonal selection limit (Fig. 5, *blue dashed line*) each galaxy lies. We also show the colors of a few Bruzual & Charlot (2003) model tracks, illustrating that the break parameter passes through zero at $z = 2.7$ for a wide range of galaxy types.

We have divided the sources into three magnitude ranges: (a) $19 \leq F606W_{AB} < 22.75$, where all but one of the galaxies (with $F606W_{AB} = 22.69$) are identified, (b) $22.75 \leq F606W_{AB} < 23.5$, where the galaxy identifications are 97% complete, and (c) $23.5 \leq F606W_{AB} < 24.5$, where a substantial number of $z > 2.7$ galaxies enter the sample. The galaxies follow a remarkably well defined track in all the panels. In Figure 6a only the two AGNs have $z > 2.7$, and, as we have discussed above, both lie close to the zero U break parameter. In Figure 6b we see the appearance of the

Fig. 4.—Redshift vs. (*a*) F435W$_{AB}$ magnitude for the F435W$_{AB}$ < 25 sample, (*b*) F606W$_{AB}$ magnitude for the F606W$_{AB}$ < 24 sample, (*c*) F850LP$_{AB}$ magnitude for the F850LPW$_{AB}$ < 24 sample, and (*d*) $K_{s, AB}$ magnitude for the $K_{s, AB}$ < 23 sample. AGNs, defined as sources with rest-frame hard or soft X-ray luminosities >10^{42} ergs s^{-1}, are denoted by large red squares. The fraction of unidentified sources per 0.5 mag bin is shown in histogram form at the bottom of each plot (label is on the right-hand *y*-axis).

first $z > 2.7$ galaxy, which has a magnitude of F606W$_{AB}$ = 23.4. This galaxy lies above the selection limit, while the extended galaxy+AGN discussed above, which also appears in this figure, does not.

In Figure 6*c* the $z = 2.7$–3.4 sources become more common. Twelve lie above the selection limit and five lie below, of which only two lie fairly far below, including one further extended source with a weak AGN. Of particular note is the relatively small number of sources in the lower right quadrant in all three panels. This is not consistent with the work of Le Fèvre et al. (2005) and Paltani et al. (2007), who claim to have discovered a significantly larger galaxy population at high redshifts ($z \sim 3$) than had previously been identified, particularly at bright magnitudes. They found that their $2.7 \leq z \leq 3.4$ galaxies were mainly located near the boundary used to isolate LBGs in their $u - g$, $g - r$ color-color diagram, so they adopted a very conservative diagonal limit for their selection criterion at the expense of more contamination from low-redshift galaxies. We find no evidence for a strong population of this type of galaxy.

We can perform a similar analysis at lower redshifts using the *GALEX* magnitudes. In Figures 7*a* and 7*c* we show the LBG selection of $0.6 \leq z < 1.4$ galaxies (*blue solid lines*) using the (FUV−NUV)$_{AB}$ versus (NUV−F435W)$_{AB}$ color-color diagram.

In Figures 7*b* and 7*d* we show the selection of $1.4 \leq z < 2.7$ galaxies (*blue solid lines*) using the (NUV−U)$_{AB}$ versus (U−F606W)$_{AB}$ color-color diagram. In both cases we have used an equivalent selection to that of the high-redshift LBGs. For Figures 7*a* and 7*c* we include all sources with NUV$_{AB}$ < 23.75, which is 100% spectroscopically complete. For Figures 7*b* and 7*d* we include all sources with U_{AB} < 23.75, which is 97% spectroscopically complete. An NUV$_{AB}$ = 23.75 magnitude limit at $z = 1$ corresponds to an F606W limit of 26 at $z = 3$, so these near-ultraviolet samples extend to much lower luminosities than the F606W sample. The samples have been divided into extended (<0.5; Figs. 7*a* and 7*b*) and compact (>0.5; Figs. 7*c* and 7*d*) using the SExtractor stellarity index, as measured in the ACS F850LP image.

The color-color diagrams pick out nearly all of the galaxies above the selection limits ($z > 0.6$ or $z > 1.4$). Figures 7*a* and 7*c* suggest that the (NUV−F435W)$_{AB}$ constraint could be relaxed without increasing the selection contamination. It can be seen from Figures 5 and 6 that the vertical constraint can also be relaxed at higher redshifts, except as a way to minimize the star contamination problem when the LBG selection is applied without a compactness measurement. (Fig. 5*b* shows how the star track edges into the selection region; some of these can be eliminated by the
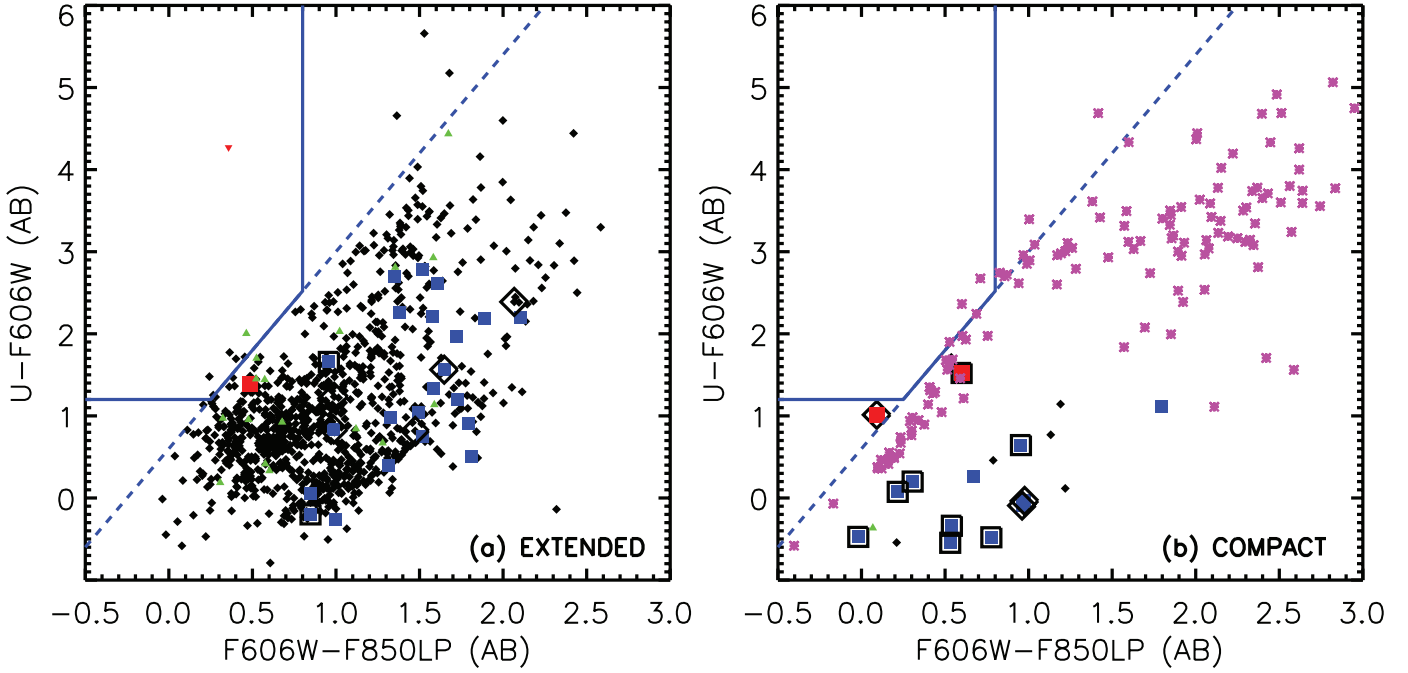
Fig. 5.—The $(U - F606W)_{AB}$ vs. $(F606W - F850LP)_{AB}$ color-color diagram for our nearly spectroscopically complete $F606W_{AB} < 23.5$ sample ($z \leq 2.7$ galaxies: *black diamonds*; $z > 2.7$ galaxies: *red inverted triangles*; spectroscopically identified stars: *purple stars*; unidentified sources: *green triangles*), divided into (*a*) extended and (*b*) compact sources, depending on whether the SExtractor stellarity index in the ACS F850LP image is less than or greater than 0.5, respectively. All of the spectroscopically identified stars fall in (*b*). The large squares are AGNs (*blue for $z \leq 2.7$; red for $z > 2.7$*). Those AGNs classified as broad-line AGNs are enclosed in larger black squares, and those with high-excitation emission lines (C IV or [Ne V]) are enclosed in larger black diamonds. The blue solid lines mark where LBGs with $2.7 \leq z \leq 3.4$ would be searched for in a color-color preselection.

[F606W−F850LP]$_{AB} < 0.8$ constraint.) From Figure 7*d* we see that star contamination can be substantial if we use the LBG method to select $z \sim 1$ galaxies without compactness information.

The color selections in Figure 7 are also surprisingly good at picking out AGNs, including many of the broad-line AGNs, suggesting that some of these have strong Lyman breaks also. However, as with the high-redshift sample, there are AGNs that would be missed by the color selection. Cowie et al. (2008) discusses the implications of this for the production of the metagalactic ionizing flux.

We use the 100% complete $NUV_{AB} < 23.75$ sample of Figures 7*a* and 7*c* to assess the selection completeness and the selection contamination. Of the 86 galaxies in that sample with $z > 0.6$, 79 are selected by the cuts

$$(FUV - NUV)_{AB} > 1.2, \qquad (4)$$

and

$$(FUV - NUV)_{AB} > (NUV - U)_{AB} \times 2.4 + 0.6. \qquad (5)$$

This gives a selection completeness of 92%. Note that one of the omitted sources is an X-ray luminous broad-line quasar. Since the above cuts pick out 116 sources, the selection contamination by sources with $z \leq 0.6$ is 32%.

We conclude that while there may be a very small number of unusual sources where AGN contamination (or some other cause) moves the source outside the selection region, more than 90% of galaxies in the desired redshift range will be picked out by the LBG selection. While we have based our analysis on the low-redshift sample, the selection completeness should only be higher at high redshifts, where the effects of the Lyα forest accentuate the LBG selection.

4.2. *The BzK Selection*

Daddi et al. (2004) proposed a NIR selection technique for finding high-redshift galaxies defined by

$$BzK \equiv (z - K_s)_{AB} - (B - z)_{AB}. \qquad (6)$$

With this relation, $z > 1.4$ star-forming galaxies can be identified using the criterion $BzK \geq -0.2$, while $z > 1.4$ old stellar systems can be isolated using the criteria $BzK < -0.2$ and $(z - K_s)_{AB} > 2.5$. Daddi et al. (2004) applied the technique to the K20 ($K_{s, AB} < 21.8$) survey (Cimatti et al. 2002). This survey includes a 32 arcmin^2 region in the GOODS-S, where 328 of the 347 sources have spectroscopic redshifts, and a 19 arcmin^2 area centered on the QSO 0055-269 at $z = 3.656$, where 176 of the 198 sources have spectroscopic redshifts. They also utilized photometric redshifts, which make up a sizeable fraction of their $z > 1.4$ sample. Daddi et al. (2004) found that their BzK selection criteria did very well at selecting $z > 1.4$ galaxies; moreover, only about 12% of their final sample were lower redshift "interlopers." Some of this contamination was due to AGNs. They also checked their criteria on two deeper samples, a spectroscopic sample to $K_{s, AB} = 22.4$ from the Gemini Deep Deep Survey (GDDS; Abraham et al. 2004) and a photometric sample to $K_{s, AB} = 23.8$ from ISAAC imaging of the same GOODS-S region covered by the K20 survey. These samples supported the continued validity of the method for magnitudes fainter than $K_{s, AB} = 21.8$, although the GDDS sample of $z > 1.4$ galaxies was small, and the ISAAC sample did not have spectroscopic redshifts. (Popesso et al. [2008] have since increased the number of spectroscopic redshifts in the GOODS-S field using VIMOS. However, it does not appear that they are using a K_s-selected sample in their Fig. 10 BzK diagram.)

Because it is important to understand how well the BzK selection works, especially before applying the method to extremely
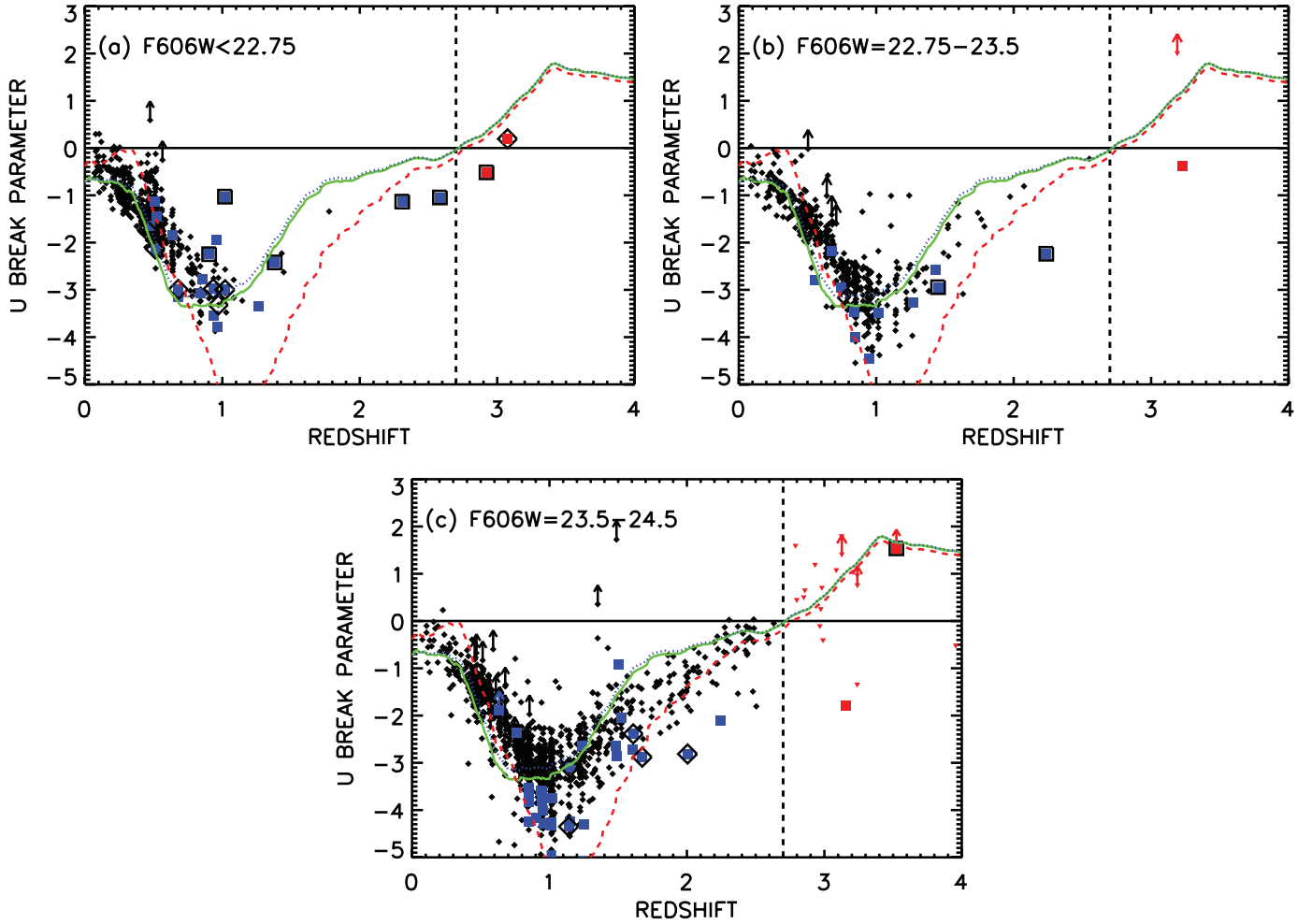
Fig. 6.—*U*-break parameter $[(U - F606W)_{AB} - (F606W - F850LP)_{AB} \times 2.4 - 0.6]$ vs. redshift for every $F850LP_{AB} \geq 19$ galaxy with a spectroscopic redshift (*black for z $\leq$ 2.7*; *red for z > 2.7*). The large squares are AGNs (*blue for z $\leq$ 2.7*; *red for z > 2.7*). The broad-line AGNs are shown enclosed in larger black squares. Sources with high-excitation emission lines (C IV or [Ne V]) are shown enclosed in larger black diamonds. The arrows show 2 σ lower limits. (*a*) $19 \leq F606W_{AB} < 22.75$, where every galaxy has a spectroscopic redshift; (*b*) $22.75 \leq F606W_{AB} < 23.5$, where 97% of the galaxies have redshifts and where there is only one z > 2.7 galaxy; and (*c*) $23.5 \leq F606W_{AB} < 24.5$, where z > 2.7 sources begin to appear in significant numbers. The dashed vertical line marks the z = 2.7 lower limit of the LBG redshift selection. The curves show the expected break parameters from Bruzual & Charlot (2003) models for exponentially declining star formation rates with decline times of 10^9 yr (*red dashed line*), 5×10^9 yr (*green solid line*), and 10^{10} yr (*blue dotted line*), solar metallicities, and ages equal to the age of the universe at that redshift.

large samples, such as those being generated by the UKIRT Infrared Deep Sky Survey (UKIDSS; Lane et al. 2007), several other groups have also tried to test its reliability. In most of these cases the authors have compared the locations of the sources in the *BzK* diagram with their photometric redshift estimates (e.g., Kong et al. 2006; Grazian et al. 2007; Quadri et al. 2007). However, the difficulty with this approach is that the colors used to construct the *BzK* diagram and the photometric redshift estimates are not independent.

4.2.1. *Our Nearly Spectroscopically Complete Sample*

We can investigate the reliability of the *BzK* method using our nearly complete, large spectroscopic sample in the GOODS-N region. The area covered by our sample is substantially larger than that of the K20 survey (145 arcmin^2 vs. 51 arcmin^2), although the $K_{s, AB}$ limit to which we are complete to the same level as K20 is shallower ($K_{s, AB} = 21.4$ vs. $K_{s, AB} = 21.8$).

In Figure 8 we restrict our sample to the magnitude range $15 < K_{s, AB} \leq 21$ (the lower limit is to avoid saturation problems, which would lead to incorrect colors). Of the 964 sources in this sample, only 45 have not been spectroscopically identified (*green triangles*). We use red symbols (galaxies, *inverted triangles*; AGNs,

large red squares) to show the z > 1.4 sources, and we use black diamonds for galaxies and large blue squares for AGNs to show the z $\leq$ 1.4 sources. We denote the spectroscopically identified stars with purple stars, and we use large purple open squares to show sources whose SExtractor stellarity index, as measured in the F850LP image, is >0.5 (i.e., compact). This parameter identifies all of the spectroscopic stars and many of the AGNs as compact sources. We see a very tight sequence for the z $\leq$ 1.4 galaxies. We also see that the *BzK* criterion (*diagonal line*) does a reasonable job of separating most of the sources into the correct redshift regimes. However, we note that to this magnitude limit only one spectroscopically identified galaxy at z > 1.4 lies in the passive galaxies region of the diagram (to the right of the diagonal line and above the horizontal line).

There are 15 spectroscopically identified z > 1.4 sources to the left of the diagonal line and only three (one of which lies in the z > 1.4 passive galaxy region) to the right of the diagonal line. Thus, the *BzK* selection of z > 1.4 star-forming galaxies (i.e., excluding the z > 1.4 source in the passive galaxy region) has a high selection completeness (88%).

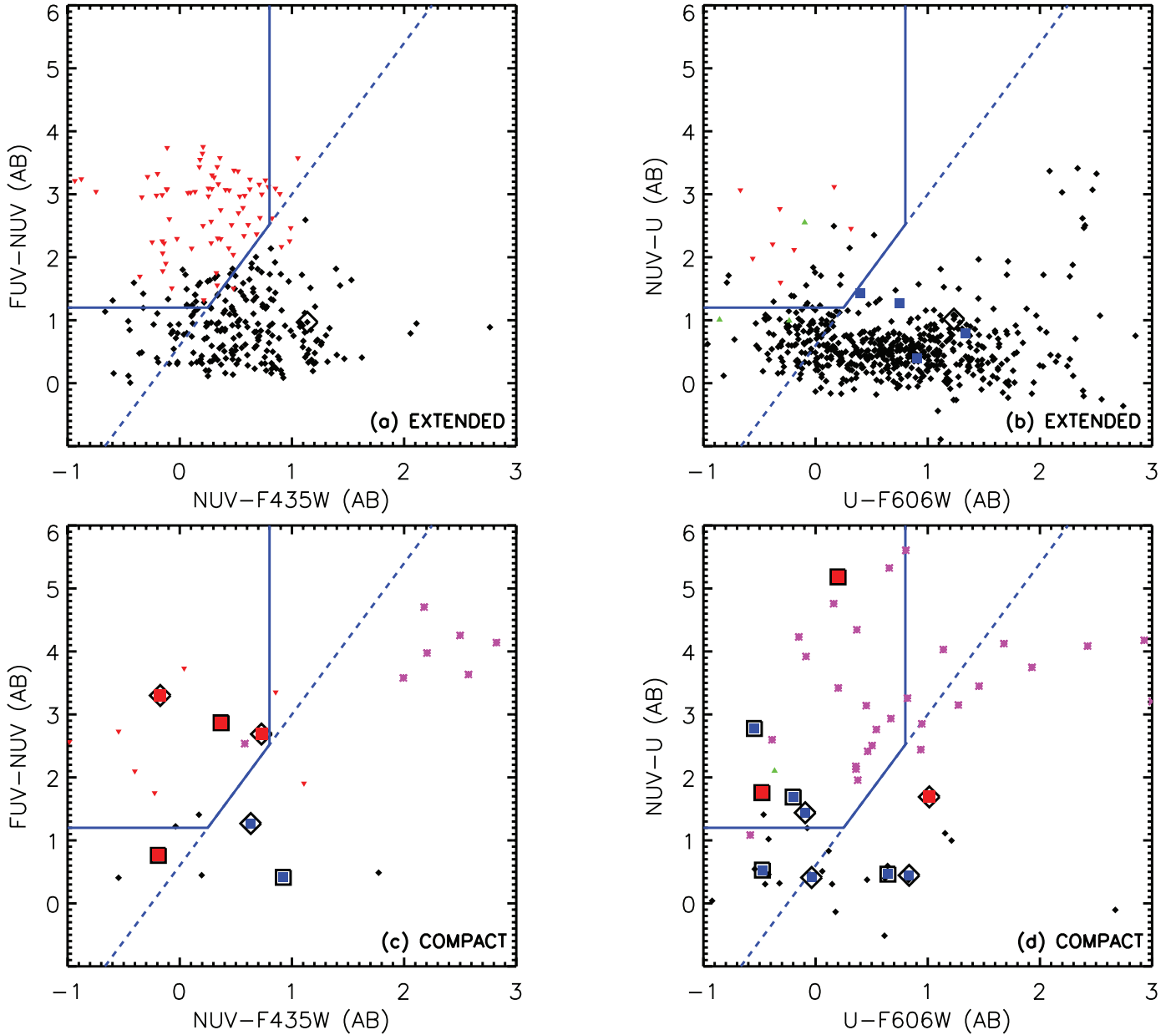We can also estimate the minimum and maximum selection contamination by taking into account the 45 spectroscopically

Fig. 7.—(*a*) Extended and (*c*) compact (FUV−NUV)$_{AB}$ vs. (NUV−F435W)$_{AB}$ and (*b*) extended and (*d*) compact (NUV−U)$_{AB}$ vs. (U−F606W)$_{AB}$ color-color diagrams for our 100% spectroscopically complete NUV$_{AB}$ < 23.75 sample (*a* and *c*) and our 97% spectroscopically complete U_{AB} < 23.75 sample (*b* and *d*). The extended and compact designations depend on whether the SExtractor stellarity index in the ACS F850LP image is less than or greater than 0.5, respectively. In (*a*) and (*c*) the black diamonds are galaxies with spectroscopic redshifts $z \leq 0.6$, the red inverted triangles are galaxies with spectroscopic redshifts $z > 0.6$, the large squares are AGNs (*blue for* $z \leq 0.6$; *red for* $z > 0.6$), and the blue solid lines mark where LBGs with $z > 0.6$ would be searched for in a color-color preselection. In (*b*) and (*d*) the black diamonds are galaxies with spectroscopic redshifts $z \leq 1.4$, the red inverted triangles are galaxies with spectroscopic redshifts $z > 1.4$, the large squares are AGNs (*blue for* $z \leq 1.4$; *red for* $z > 1.4$), the blue solid lines mark where LBGs with $z > 1.4$ would be searched for in a color-color preselection, and the green triangles are the unidentified sources. All of the spectroscopically identified stars (*purple stars*) fall in the compact panels. In all panels the broad-line AGNs are shown enclosed in larger black squares, and sources with high-excitation emission lines (C IV or [Ne V]) are shown enclosed in larger black diamonds.

unidentified sources in the sample. Thirteen of these lie in the $z > 1.4$ star-forming region, two in the $z > 1.4$ passive galaxies region, and the remaining 30 in the $z \leq 1.4$ region.

We first consider the $z \leq 1.4$ region of the diagram. Here there are two spectroscopically identified $z > 1.4$ sources (interlopers) and 768 spectroscopically identified $z \leq 1.4$ sources. If we assume that all 30 of the unidentified sources in the $z \leq 1.4$ region do in fact have $z \leq 1.4$, then we obtain a minimum selection contamination of 0.25%. If we instead assume that all 30 of the unidentified sources in the $z \leq 1.4$ region actually have $z > 1.4$ (interlopers), then we obtain a maximum selection contamination of 4%.

We next consider the $z > 1.4$ star-forming region of the diagram (i.e., we are not considering the $z > 1.4$ passive region). Here there are 14 spectroscopically identified $z \leq 1.4$ sources (interlopers) and 15 spectroscopically identified $z > 1.4$ sources. If we assume that all 13 of the unidentified sources in the $z > 1.4$ star-forming region do in fact have $z > 1.4$, then we obtain a minimum selection contamination of 33%. If we instead assume that all 13 of the unidentified sources in the $z > 1.4$ star-forming region actually have $z \leq 1.4$ (interlopers), then we obtain a maximum selection contamination of 64%.

We conclude that at these magnitudes the *BzK* selection of $z > 1.4$ star-forming galaxies has a high selection completeness
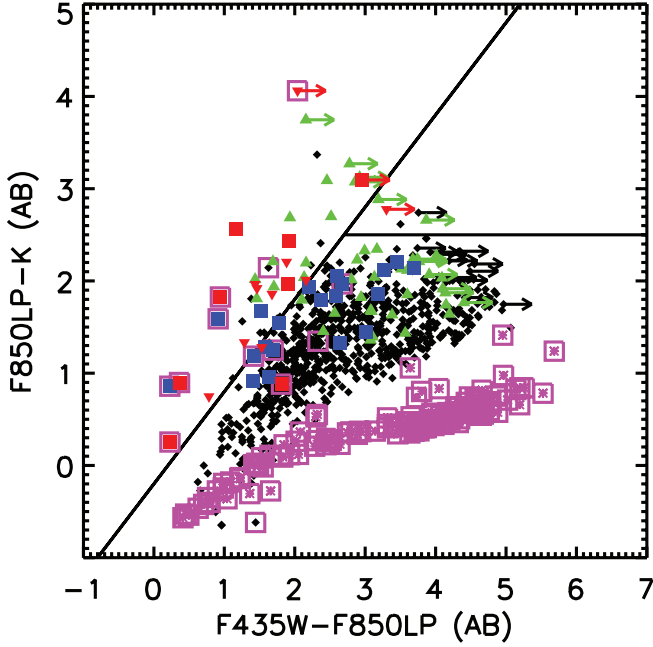
FIG. 8.—The $(F850LP - K_s)_{AB}$ vs. $(F435W\text{-}F850LP)_{AB}$ color-color diagram for the $15 < K_s$, AB ≤ 21 sample. The $z \leq 1.4$ galaxies are denoted by black diamonds, and the $z > 1.4$ galaxies are denoted by red inverted triangles. AGNs are denoted by large squares (*blue for $z \leq 1.4$; red for $z > 1.4$*). The unidentified sources are denoted by green triangles. Sources with only $2\,\sigma$ lower limits in F435W are denoted by right-pointing arrows. Spectroscopically identified stars are denoted by purple stars. The large purple open squares show sources whose SExtractor stellarity index measured on the F850LP image is >0.5. The black diagonal line shows the $BzK \geq -0.2$ selection of $z > 1.4$ star-forming galaxies. This line combined with the horizontal line shows the $BzK \geq -0.2$, $(F850LP - K_s)_{AB} > 2.5$ selection of passive galaxies at $z > 1.4$. Both were proposed by Daddi et al. (2004).

FIG. 9.—The $(F850LP - K)_{s, AB}$ vs. $(F435W\text{-}F850LP)_{AB}$ color-color diagram for the $15 < K_s$, AB ≤ 22.8 sources with redshifts from Reddy et al. (2005). The $z \leq 1.4$ galaxies are denoted by black diamonds, and the $z > 1.4$ galaxies are denoted by red inverted triangles. AGNs are denoted by large squares (*blue for $z \leq 1.4$; red for $z > 1.4$*). The diagonal line shows the $BzK \geq -0.2$ selection of $z > 1.4$ star-forming galaxies proposed by Daddi et al. (2004).

but a substantial selection contamination. Thus, *BzK* is effective at picking out high-redshift candidates, but spectroscopic follow-up is crucial to weed out the substantial number of interlopers.

4.2.2. *Our Fainter Magnitude Sample*

It is important to try to push the *BzK* analysis to fainter magnitudes, even with the increasing spectroscopic incompleteness. Reddy et al. (2005) tested the *BzK* selection on a fairly substantial, albeit not uniformly selected, high-redshift spectroscopic sample. They spectroscopically observed a $z \sim 2$ sample in the GOODS-N field selected using the observed $U_n G\mathcal{R}$ colors to a limiting AB magnitude of $\mathcal{R} = 25.5$. These $z \sim 2$ galaxies were selected to be actively star-forming galaxies with the same range in UV properties and extinctions as the LBGs at $z \sim 3$. Adelberger et al. (2004) and Steidel et al. (2004) named sources selected in this way "BX" ($2.0 \leq z \leq 2.6$) and "BM" ($1.5 \leq z \leq 2.0$) galaxies.

Reddy et al. (2005) then used a moderately deep K_s image (5 σ limit of $K_{s, AB} \sim 23.8$) covering ~ 72.3 arcmin^2 to put their galaxies on a $K_{s, Vega} \leq 21$ ($K_{s, AB} \leq 22.8$) *BzK* diagram (see their Fig. 12). For consistency, in Figure 9 we replot their spectroscopic sample on a *BzK* diagram using our deeper imaging data but restricting to their range $15 < K_{s, AB} \leq 22.8$. We have coded the data points so the $z \leq 1.4$ galaxies (*black diamonds*) can be differentiated from the $z > 1.4$ galaxies (*red inverted triangles*). We denote the AGNs (rest-frame hard or soft X-ray luminosities >10^{42} ergs s^{-1}) with large squares (*blue for $z \leq 1.4$; red for $z > 1.4$*). For this fainter spectroscopic sample the *BzK* selection still seems to do a reasonably good job of separating the high-redshift galaxies from the low-redshift galaxies, with only a small amount of contamination in either direction (five $z > 1.4$ sources
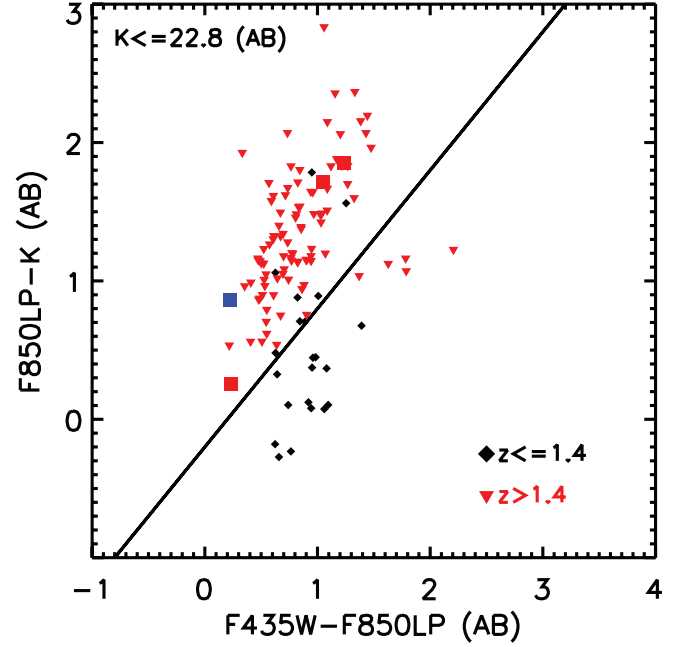
in the low-redshift region; nine $z \leq 1.4$ sources in the high-redshift region, including one AGN). The *BzK z > 1.4* star-forming galaxy selection completeness is 91% for this sample.

Reddy et al. (2005) claim that the *BzK* selection completeness decreases slightly at fainter magnitudes, missing about 20% of the $K_{s, AB} > 22.8$ BX/BM galaxies with spectroscopic redshifts $1.4 < z < 2.6$. They point out that a significant fraction of these have colors that place them within $\lesssim 0.2$ mag of the selection window, which is comparable to the photometric uncertainties. Reddy et al. (2005) also found that 11% of their BX/BM *candidates* with K_s data were undetected to $K_{s, AB} = 24.3$ (3 σ). Thus, they conclude that high-redshift sources may be missed from the *BzK* selection because of photometric scatter or because of insufficiently deep K_s data.

Although we are unable to investigate these issues with a nearly spectroscopically complete sample, we can use just our spectroscopically identified sample to study the selection completeness and selection contamination with increasing magnitude. In Figure 10 we plot two redshift samples separately: (*a*) $z \leq 1.4$ sources only and (*b*) $z > 1.4$ sources only. For each we show three magnitude intervals ($15 < K_{s, AB} \leq 21$, *green inverted triangles*; $21 < K_{s, AB} \leq 23$, *red triangles*; $23 < K_{s, AB} \leq 24$, *black diamonds*; note that the sources heavily overlap).

With increasing magnitude there is an increasing buildup of sources along the *BzK* boundary for both redshift intervals. However, in contrast to the Reddy et al. (2005) conclusion that a substantial fraction of $z > 1.4$ sources are missed by the *BzK* selection, we find that the selection completeness is extremely good. In total, 254 of the 267 sources with $1.4 < z < 2.8$ (95%) are found with the *BzK* selection. For the faintest magnitude interval $23 < K_{s, AB} \leq 24$, 69 of the 74 sources with $1.4 < z < 2.8$ (93%) are found. The different conclusion is probably a consequence of the deeper K_s image used here and the corresponding increase in precision in the determination of the *BzK* parameter.
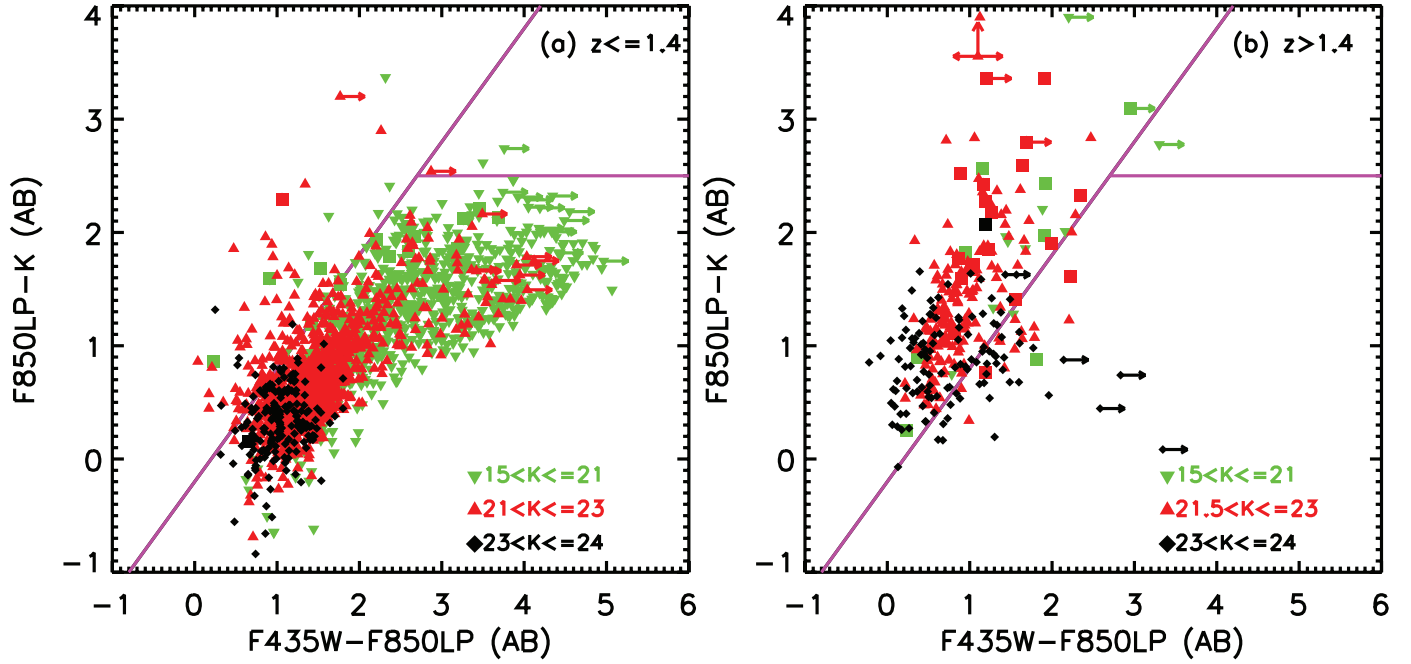
Fig. 10.—The $(F850LP - K_s)_{AB}$ vs. $(F435W\text{-}F850LP)_{AB}$ color-color diagram for all of the spectroscopically identified $15 < K_{s,\,AB} \le 24$ sources with redshifts (a) $z \le 1.4$ and (b) $z > 1.4$. AGNs are denoted by large squares. Sources with $(F850LP - K_s)_{AB}$ colors redder than 3.9 are shown at that value. The sources are color- and symbol-coded by magnitude range (see figure legend). The diagonal line shows the $BzK \ge -0.2$ selection of $z > 1.4$ star-forming galaxies. This line combined with the horizontal line shows the $BzK \ge -0.2$, $(F850LP - K_s)_{AB} > 2.5$ selection of passive galaxies at $z > 1.4$. Both were proposed by Daddi et al. (2004).

To quantitatively assess what fraction of the spectroscopically identified sources are interlopers on either side of the BzK boundary, in Figure 11 we plot redshift histograms of (a) sources that satisfy the BzK $z > 1.4$ star-forming galaxy criterion and (b) sources that do not. Both figures are divided into the same $K_{s,\,AB}$ magnitude intervals used in Figure 10. AGNs are denoted by solid shading. Since there are such a large number of galaxies at $z \le 1.4$, in Figure 11b we only show the AGNs at $z \le 1.4$. In Figure 11a the sources to the left of the vertical line can be thought of as interlopers in the $z > 1.4$ BzK star-forming region. The contamination is substantial, about 35% in the $21 < K_{s,\,AB} \le 23$ interval. In Figure 11b the sources to the right of the vertical line can be thought of as interlopers in the $z \le 1.4$ region (or as $z > 1.4$ sources missed by the BzK star-forming galaxy selection).

This is consistent with our results from using our highly spectroscopically complete sample at $15 < K_{s,\,AB} \le 21$. A BzK selection picks out nearly all the $z > 1.4$ sources but with a substantial contamination by lower redshift objects. However, it must be remembered that the spectroscopically unidentified sources at these fainter magnitudes may contain substantial biases and that the number of unidentified sources in these fainter magnitude ranges is very large: 1016 unidentified sources (vs. 1331 identified) at $21 < K_{s,\,AB} \le 23$ and 2083 unidentified sources (vs. 311 identified) at $23 < K_{s,\,AB} \le 24$.

4.3. H⁻

The minimum at 1.6 μm in the opacity of the H⁻ ion present in the atmospheres of cool stars (e.g., John 1988) is seen as a spectral "bump" in the SEDs of all but the youngest ($\sim$1 Myr) composite stellar populations (see Sawicki 2002, Fig. 1). Because of its strength and near universality, Simpson & Eisenhardt (1999) and Sawicki (2002) proposed that the 1.6 μm bump could be used to obtain photometric redshift measurements for galaxies. However, in using MIR colors as a redshift indicator, one needs to be concerned about the effects of AGN contamination.

Since optically selected luminous AGNs often have red power-law SEDs (e.g., Neugebauer et al. 1979; Elvis et al. 1994), several groups have used this characteristic to try to select AGNs in deep surveys using IRAC data (Alonso-Herrero et al. 2006; Donley et al. 2007). Other authors (Lacy et al. 2004; Stern et al. 2005; Hatziminaoglou et al. 2005; Sajina et al. 2005) have proposed that AGNs might be found in a different portion of MIR color-color space than star-forming galaxies. Both of these approaches have been suggested as ways to locate AGNs that may be missed by other techniques.

In Figure 12 we show the $(m_{3.6\,\mu m} - m_{4.5\,\mu m})_{AB}$ versus $(m_{5.8\,\mu m} - m_{8.0\,\mu m})_{AB}$ color-color diagram for all the spectroscopically identified sources in Table 1 with $m_{8.0\,\mu m,\,AB} < 22$ and (a) a rest-frame hard or soft X-ray luminosity $<10^{42}$ ergs s^{-1} and a radio power $<10^{31}$ ergs s^{-1} Hz^{-1}, (b) a rest-frame hard or soft X-ray luminosity $\ge 10^{42}$ ergs s^{-1}, and (c) a rest-frame hard or soft X-ray luminosity $<10^{42}$ ergs s^{-1} and a radio power $\ge 10^{31}$ ergs s^{-1} Hz^{-1}. We apply the $m_{8.0\,\mu m,\,AB} < 22$ limit because at fainter magnitudes the S/N at 8 μm is poor and the colors would not be reliable. The $K_{s,\,AB} < 24.5$ sample should include all of the $m_{8.0\,\mu m,\,AB} < 22$ sources, since sources are fainter at 8 μm. The spectroscopic completeness of the $m_{8.0\,\mu m,\,AB}$ sample is 94% at $m_{8.0\,\mu m,\,AB} = 21$ and 79% at $m_{8.0\,\mu m,\,AB} = 22$. An ultraluminous infrared galaxy ($L_{FIR} \ge 4 \times 10^{45}$ ergs s^{-1}) that follows the FIR-radio correlation (Condon 1992) would have a radio power of $\sim 4.8 \times 10^{30}$ ergs s^{-1} Hz^{-1} (Barger et al. 2007). Thus, it is likely that any source with a radio power $\ge 10^{31}$ ergs s^{-1} Hz^{-1} is a radio AGN, or at least a very unusual source, which is why we show these sources separately in Figure 12c. We refer to these as high radio power sources hereafter, but their colors are clearly very similar to those of the rest of the sample. In Figure 12b we enclose in large black squares any source with a rest-frame hard or soft X-ray luminosity $\ge 10^{44}$ ergs s^{-1} (X-ray quasar luminosity).

We mark with the green dashed lines the region considered to contain broad-line AGNs by Stern et al. (2005; note that their
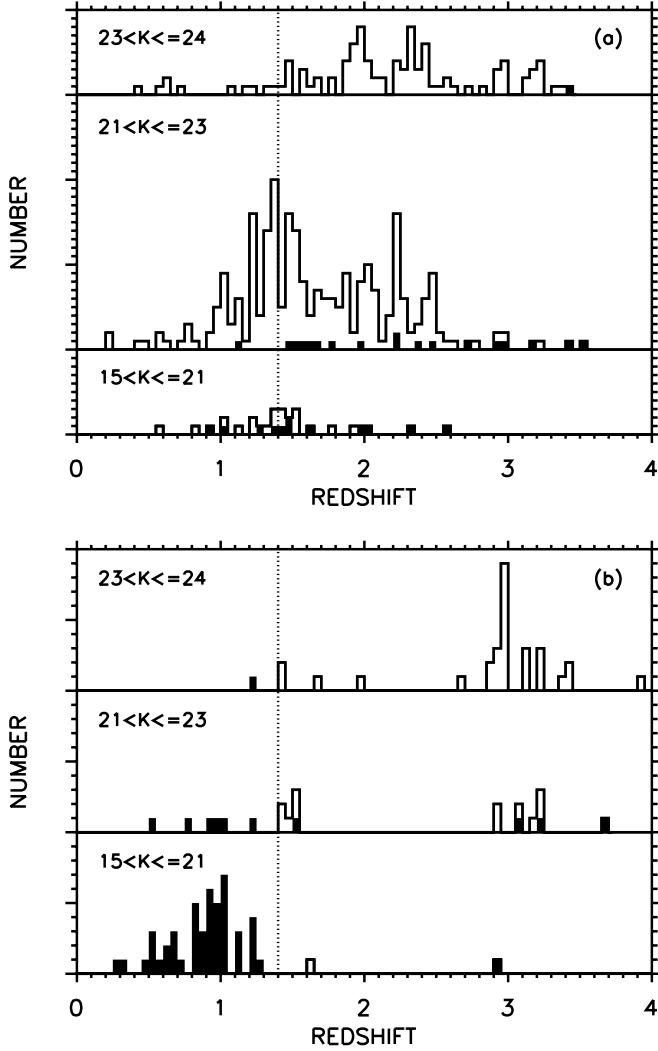
Fig. 11.—Redshift histograms by magnitude interval (see figure labels) for the spectroscopically identified $15 < K_{s,AB} \leq 24$ sources. AGNs are denoted by shading. The dotted vertical lines show $z = 1.4$. (a) $BzK \geq -0.2$, the selection of $z > 1.4$ star-forming galaxies proposed by Daddi et al. (2004). (b) $BzK < -0.2$ and $(F850LP - K_s)_{AB} \leq 2.5$ (the latter constraint to exclude passive galaxies at $z > 1.4$). Here only AGNs are shown at $z \leq 1.4$ due to the very large numbers of galaxies at $z \leq 1.4$. Each tick mark on the y-axis represents one source in both panels.

Fig. 1 shows a few broad-line AGNs and most of the narrow-line AGNs lying outside this region). We can see from our data that this color-color plot is quite poor at picking out lower luminosity AGNs (see also Barmby et al. 2006; Treister et al. 2006; Donley et al. 2007; Cardamone et al. 2008), while also missing one of the more luminous X-ray AGNs and six of the high radio power sources. It cleanly selects just a few additional AGNs that are not already identified as AGNs based on their X-ray properties, although there are a number of sources on the boundaries (see Fig. 12a). Thus, it appears that the AGNs are not significantly contaminating the colors of most of the galaxies, and hence the colors can be used as a redshift measure.

In Figure 12 we divide the galaxies into $z \leq 1.3$ (*black diamonds*) and $z > 1.3$ (*red inverted triangles*). These two broad redshift categories occupy fairly distinct regions of color-color space, which can be separated by the condition $(m_{3.6\,\mu m} - m_{4.5\,\mu m})_{AB} = 0.24 \times (m_{5.8\,\mu m} - m_{8.0\,\mu m})_{AB}$ (*red solid line*). We hereafter refer to this relation as the H$^-$ selection.

The H$^-$ selection is quite efficient at picking out high-redshift galaxies and AGNs, with 84 of the 94 sources with
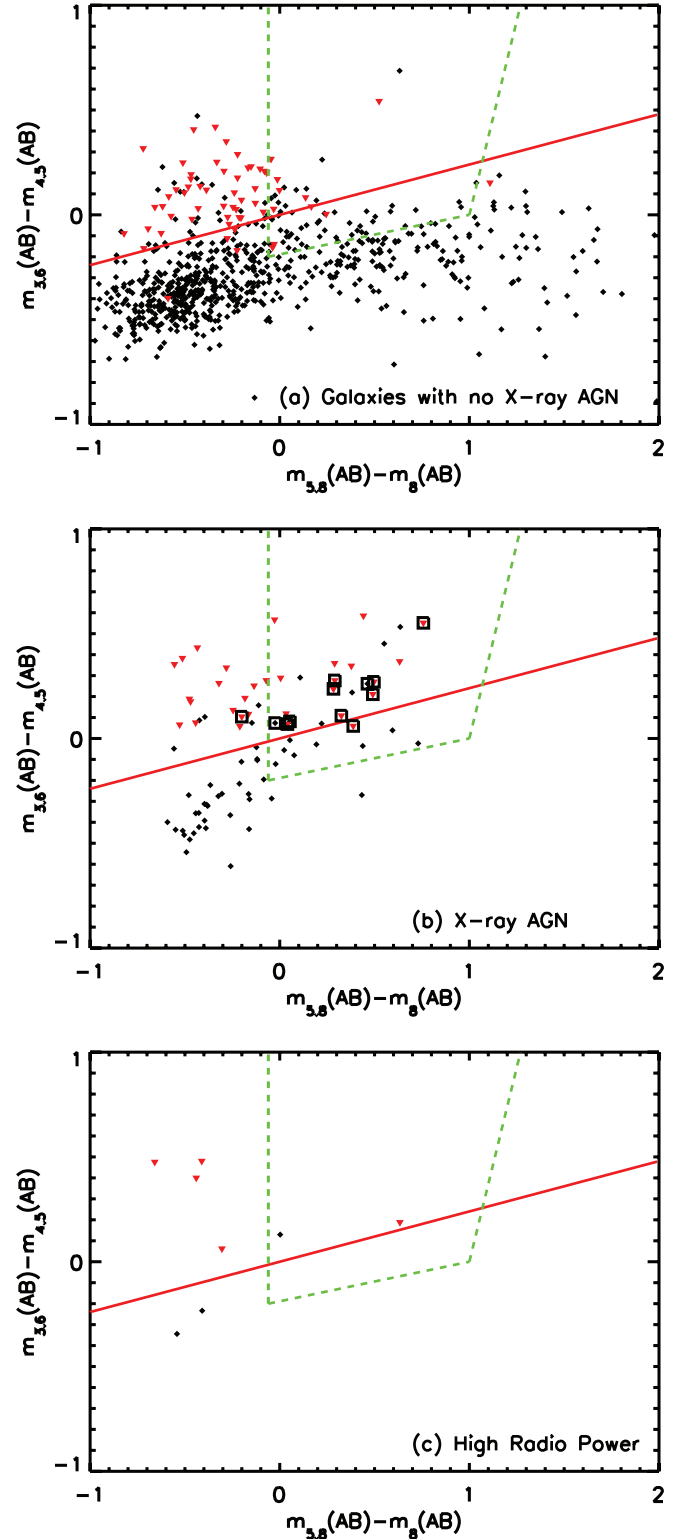
Fig. 12.—The $(m_{3.6\,\mu m} - m_{4.5\,\mu m})_{AB}$ vs. $(m_{5.8\,\mu m} - m_{8.0\,\mu m})_{AB}$ color-color diagram for all of the spectroscopically identified galaxies with $m_{8.0\,\mu m,\,AB} < 22$ and (a) a rest-frame hard or soft X-ray luminosity $< 10^{42}$ ergs s^{-1} and a radio power $< 10^{31}$ ergs s^{-1} Hz^{-1}, (b) a rest-frame hard or soft X-ray luminosity $\geq 10^{42}$ ergs s^{-1}, and (c) a rest-frame hard or soft X-ray luminosity $< 10^{42}$ ergs s^{-1} and a radio power $\geq 10^{31}$ ergs s^{-1} Hz^{-1}. Sources with $z \leq 1.3$ ($z > 1.3$) are shown as black diamonds (red inverted triangles). AGNs with quasar X-ray luminosities are enclosed in large black squares. The diagonal red solid line shows the condition $(m_{3.6\,\mu m} - m_{4.5\,\mu m})_{AB} = 0.24 \times (m_{5.8\,\mu m} - m_{8.0\,\mu m})_{AB}$, which roughly divides the sources at $z = 1.3$. The green dashed lines enclose the region where Stern et al. (2005) suggested that these MIR colors select out most broad-line AGNs.

$m_{8.0\,\mu m,\,AB} < 22$ and $z > 1.3$ satisfying it. This corresponds to a selection completeness of just under 90%. However, there is substantial selection contamination: 53 $z < 1.3$ sources also satisfy the H^- selection, giving a 39% selection contamination. Thus, as with the BzK selection, the H^- selection is a very effective means of finding the high-redshift galaxies, but in order to create a clean sample, spectroscopic follow-up is needed. (Note that Papovich [2008] suggests that an efficient way to reduce the contamination due to $z < 1.0$ interlopers is to apply an apparent magnitude cut.)

If we require the sources to satisfy both the BzK selection and the H^- selection, then we can substantially reduce the selection contamination, but at the expense of reducing the selection completeness to $\sim$80%. However, if we instead require the sources to satisfy one or the other selection, then we can find almost all of the $z > 1.4$ sources (63/64 with $m_{8.0\,\mu m,\,AB} < 22$) at the expense of a high selection contamination (about 55%). This may be the best way to generate a highly complete sample at these redshifts.

Lacy et al. (2004) suggest that interspersed colors, which are a measure of the curvature of the SED, may be more optimal in selecting AGNs. In Figure 13 we show the $(m_{3.6\,\mu m} - m_{5.8\,\mu m})_{AB}$ versus $(m_{4.5\,\mu m} - m_{8.0\,\mu m})_{AB}$ color-color diagram for all the sources in Table 1 with $m_{8.0\,\mu m,\,AB} < 22$ and (a) a rest-frame hard or soft X-ray luminosity $<10^{42}$ ergs s^{-1} and a radio power $<10^{31}$ ergs s^{-1} Hz^{-1}, (b) a rest-frame hard or soft X-ray luminosity $\geq 10^{42}$ ergs s^{-1}, and (c) a rest-frame hard or soft X-ray luminosity $< 10^{42}$ ergs s^{-1} and a radio power $\geq 10^{31}$ ergs s^{-1} Hz^{-1}. In Figure 13b we again enclose in large black squares the sources with a rest-frame hard or soft X-ray luminosity $\geq 10^{44}$ ergs s^{-1} (X-ray quasar luminosity).

We mark with green dashed lines the region considered to contain AGNs by Lacy et al. (2004). This selection is better than the Stern et al. (2005) selection in choosing luminous AGNs, but again it misses some of the lower luminosity sources, as well as three (one is just outside the boundary) of the high radio power sources. However, the galaxy contamination is severe.

In Figure 13 we divide the galaxies into $z \leq 1.6$ (black diamonds) and $z > 1.6$ (red inverted triangles). These two broad redshift categories again fall into fairly distinct regions of color-color space, which can be separated by the condition $(m_{3.6\,\mu m} - m_{5.8\,\mu m})_{AB} = 0.24 \times (m_{4.5\,\mu m} - m_{8.0\,\mu m})_{AB}$ (red dashed line). We hereafter refer to this relation as the IRAC color selection.

The IRAC color selection has a high selection completeness, selecting 47 of the 50 galaxies and AGNs with $m_{8.0\,\mu m} < 22$ and $z > 1.6$. However, once again, the contamination by lower redshift sources is substantial (about 40%), and spectroscopic follow-up is necessary to provide a clean sample. As with the H^- selection, requiring the sources to satisfy either the BzK selection or the IRAC color selection can provide an extremely complete selection (49/50 with $m_{8.0\,\mu m,\,AB} < 22$ and $z > 1.6$) at the expense of a high selection contamination (about 56%).

5. INTERGALACTIC MEDIUM TOMOGRAPHY

One interesting application of this data set is to investigate the feasibility of one of the major science projects proposed for a 30 m telescope: tomography of the IGM. The goal of the tomography project is to observe sufficient numbers of background sources (galaxies and AGNs) to have enough lines of sight to probe the distribution of the intervening gas. The Thirty Meter Telescope (TMT; Silva et al. 2007) estimated that $R \sim 24.5$ is approximately the apparent magnitude at which TMT/WFOS can obtain a spectrum at a spectral resolution of 6000 with a S/N of $\sim$30 (see their Fig. 5-12 for a simulated spectrum of an $R = 24$ galaxy observed with WFOS). The high-resolution ACS images of the present data set allow us to model this in more detail by correctly including the
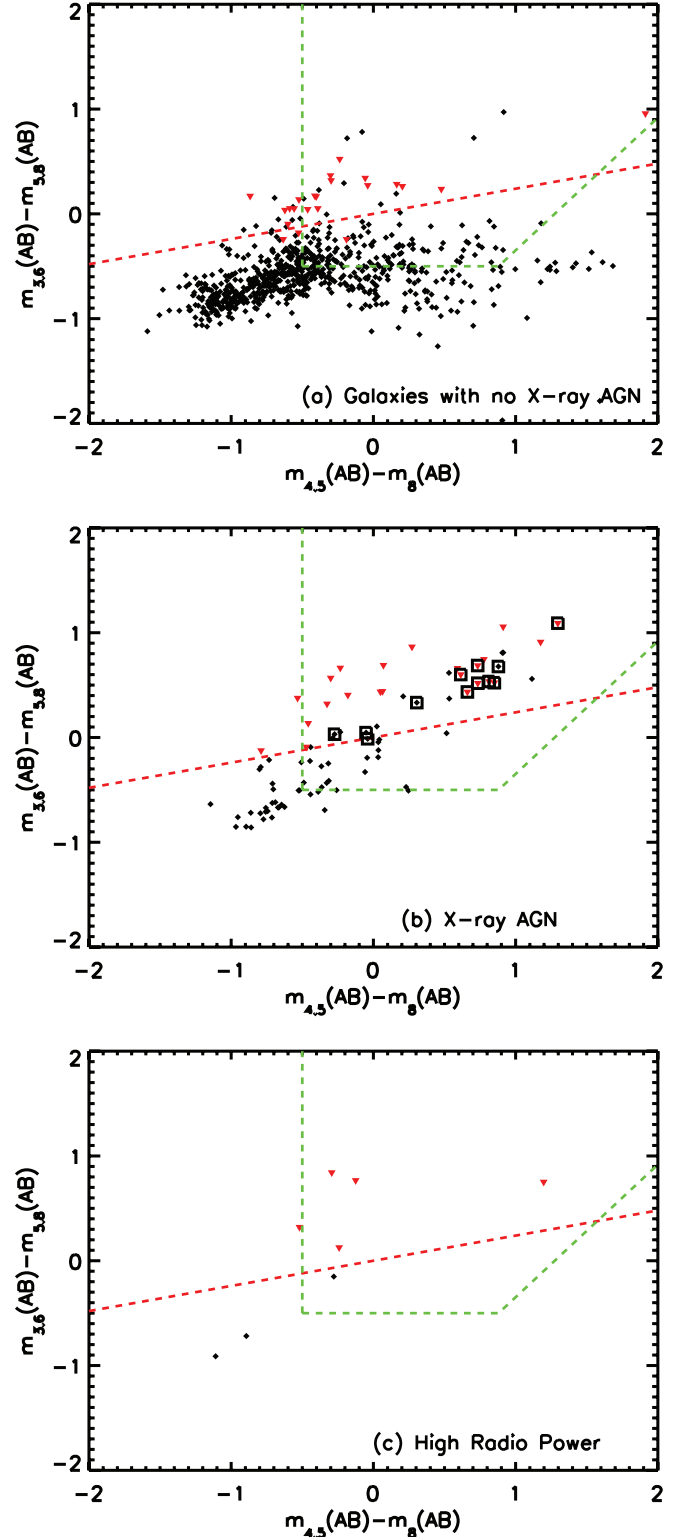

FIG. 13.— The $(m_{3.6\,\mu m} - m_{5.8\,\mu m})_{AB}$ vs. $(m_{4.5\,\mu m} - m_{8.0\,\mu m})_{AB}$ color-color diagram for all of the spectroscopically identified galaxies with $m_{8.0\,\mu m,\,AB} < 22$ and (a) a rest-frame hard or soft X-ray luminosity $<10^{42}$ ergs s^{-1} and a radio power $<10^{31}$ ergs s^{-1} Hz^{-1}, (b) a rest-frame hard or soft X-ray luminosity $\geq 10^{42}$ ergs s^{-1}, and (c) a rest-frame hard or soft X-ray luminosity $<10^{42}$ ergs s^{-1} and a radio power $\geq 10^{31}$ ergs s^{-1} Hz^{-1}. Sources with $z \leq 1.6$ ($z > 1.6$) are shown as black diamonds (red inverted triangles). AGNs with quasar luminosities are enclosed in large black squares. The diagonal red dashed line shows the condition $(m_{3.6\,\mu m} - m_{5.8\,\mu m})_{AB} = 0.24 \times (m_{5.8\,\mu m} - m_{8.0\,\mu m})_{AB}$, which roughly divides the sources at $z = 1.6$. The green dashed lines enclose the region where Lacy et al. (2004) suggested that these MIR colors select out AGNs.
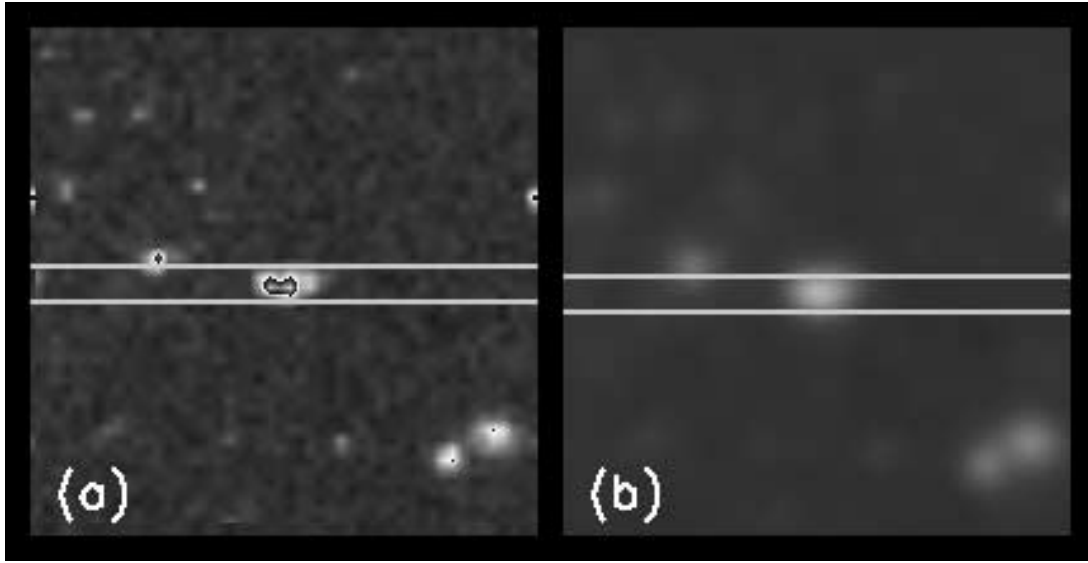
FIG. 14.—A F606W$_{AB}$ = 24 galaxy at z = 2.05 (a) before and (b) after smoothing to 0.65″ ground-based seeing. The white lines show the position of the 0.75″ wide slit.

slit losses. Here we do this by measuring the S/N, which can be obtained with an optimal positioning of each galaxy in the slit and for a given natural seeing.

For the telescope and spectrograph properties, we follow the TMT Observatory requirements document (Angeli & Roberts 2007). We take the telescope's collecting area to be 655 m^2. (The proposed Giant Magellan Telescope has an area of 368 m^2, and the exposure times would be nearly doubled.) We assume a 0.75″ wide slit and a spectral resolution of 6000 for the instrumental parameters. We take a typical sky to collection efficiency of 25%, although the peak efficiency could be slightly higher than this. We assume a 10 hr integration.

We calculate the S/N at the central wavelength (6060 Å) of the F606W filter. Longer wavelengths are in the complex OH night sky spectrum, and hence the calculation of the S/N becomes extremely wavelength-dependent. However, at 6060 Å we can assume a smooth continuum sky brightness. The choice of sky brightness is not straightforward, since it is somewhat variable and site-dependent. We adopt a continuum AB surface brightness of 21.4 mags arcsec^{-2} at this wavelength, which is based on the mean zenith V (21.7 mags arcsec^{-2}) and R (21.1 mags arcsec^{-2}) AB surface brightnesses at Cerro Paranal (Patat 2003). (The V-band sky background at Mauna Kea is similar [Krisciunas 1997].) We have also corrected for the strong emission-line contributions, and we have assumed that the galaxy is being observed at an average air mass of 1.3. The choice of the sky brightness is probably the largest uncertainty in our calculation.

We use the point-spread function determined from stars in the MOIRCS K_s image with an appropriate scaling to smooth the ACS images to the desired ground-based seeing. For our reference calculation we adopt a high-quality seeing of 0.65″, assuming that these observations would be prioritized to optimal times. We show a typical z = 2.05 galaxy with respect to the 0.75″ wide slit in Figure 14 at (a) the original ACS resolution and (b) the ground-based seeing. We place each galaxy in an optimal position in the slit and compute the S/N that would be obtained in an optimal spectral extraction of the light distribution along the slit. Because the noise is sky-dominated, the fainter portions of the light profile do not contribute much to the S/N. In Figure 15 we show the expected S/N per resolution element for all the galaxies (*black squares*) and AGNs (*large red squares*) with
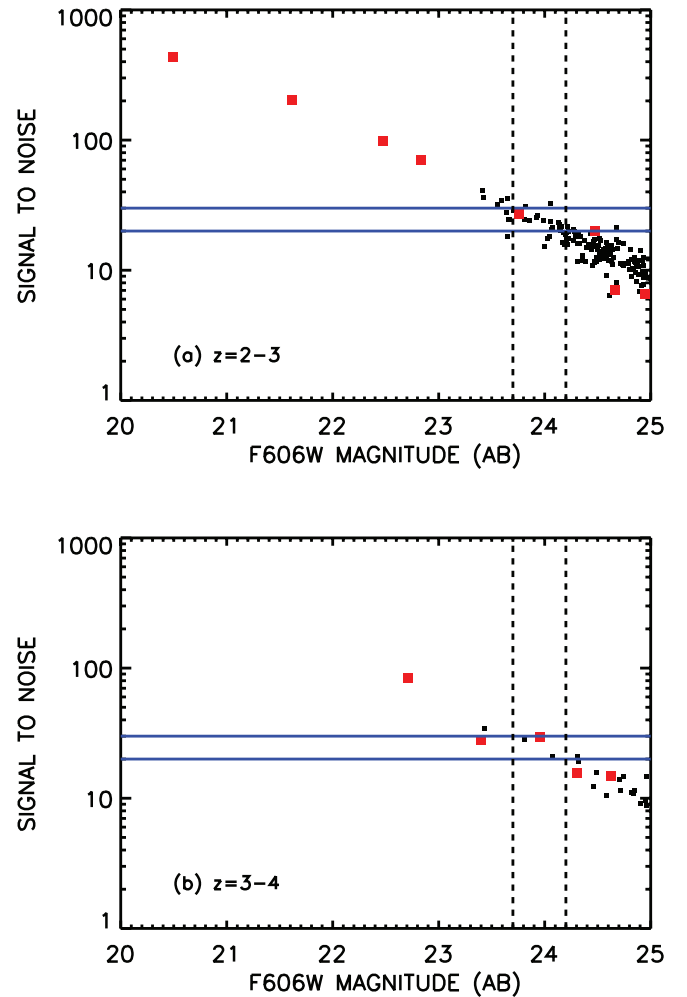

FIG. 15.—Expected S/N per resolution element vs. F606W magnitude for a 30 m telescope and an exposure time of 10 hr for the sources (galaxies and AGNs) in the redshift intervals (a) z = 2–3 and (b) z = 3–4 in the ACS GOODS-N field. The adopted seeing is 0.65″, the spectral resolution is 6000, and the slit width is 0.75″. AGNs are denoted by large red squares. The blue horizontal lines mark S/N per resolution element values of 20 and 30, and the black vertical dashed lines show the F606W AB magnitudes (24.2 and 23.7, respectively) at which these S/N values are reached for a typical galaxy.
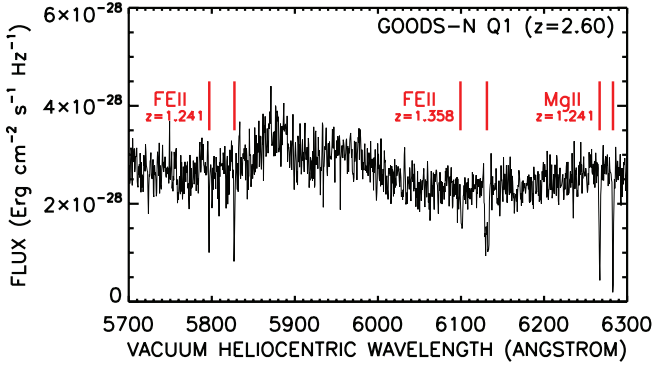
FIG. 16.—Spectrum of the brightest AGN in the $z = 2–3$ range in the ACS GOODS-N field (A. Songaila 2008, in preparation). The spectrum is a 1.5 hr exposure with a spectral resolution of 5400 obtained with a 0.75″ wide slit under 0.9″ seeing using ESI on Keck II. The spectrum is shown with pixels spaced to Nyquist sample the resolution, and the S/N is 40 per resolution element. Fe and Mg lines from two absorption systems at $z = 1.241$ and 1.358 are marked with red lines.

$F606W_{AB} < 25$ and known redshifts in the (*a*) $z = 2–3$ and (*b*) $z = 3–4$ ranges versus F606W magnitude.

We test our S/N calculation using the spectrum of the brightest AGN in the $z = 2–3$ range in the ACS GOODS-N field, the source with $F606W_{AB} = 20.5$ in Figure 15*a*. The redshift of this source is $z = 2.6$. We use a 1.5 hr spectrum obtained with the Echellette Spectrograph and Imager (ESI; Epps & Miller 1998; Sheinis et al. 2000) on the Keck II telescope from A. Songaila (2008, in preparation). The observation was made with a 0.75″ wide slit under 0.9″ seeing with some windshake. The spectral resolution is 5400. We show a segment of the spectrum around 6000 Å in Figure 16. The measured S/N is 40 in a resolution element, while our S/N calculation gives a value of 45 for a 1.5 hr exposure on a 10 m telescope at this seeing. The slight degradation may be a consequence of windshake effects on the guiding or of imperfections in the extraction of the spectrum, but overall the agreement is excellent.

The choice of S/N for the tomographic project is complex. If we simply want to identify kinematic structures, then we can tolerate lower S/N spectra, but if we wish to measure column densities and abundances, then we need high S/N spectra. In general, the strong lines that can be measured in a low-resolution spectrum with low S/N are saturated, and it is not possible to derive accurate column densities using them (e.g., Jenkins 1986; Prochaska 2007). Prochaska (2007) shows that in order to measure weak lines where useful information on the column densities can be derived, we need to detect rest-frame equivalent widths of 100 mÅ or less. For a 5 σ measurement of a 100 mÅ absorption-line system at $z = 1$, this translates to a S/N of 25 per resolution element at a spectral resolution of 6000, which seems a reasonable figure of merit. However, the surface density of sources is extremely sensitive to the limiting magnitude, since we are on the exponential tail of the galaxy distribution. In Figure 15 we show two S/N values that bracket the above figure of merit: S/N of 20 and S/N of 30 per resolution element (*blue horizontal lines*). These intersect with the galaxy track at magnitudes of $F606W_{AB} = 24.2$ and 23.7 (*vertical dashed lines*), respectively, resulting in substantially different surface densities.

To quantify this, in Figure 17 we show the cumulative surface densities of sources (galaxies and AGNs) in the ACS GOODS-N field versus $F606W_{AB}$ magnitude for the redshift intervals (*a*) $z = 2–3$ and (*b*) $z = 3–4$. We denote all sources together by black diamonds with 1 σ uncertainties (*black solid curves*) and AGNs alone by red open squares with 1 σ uncertainties (Fig. 17*a*, *red*
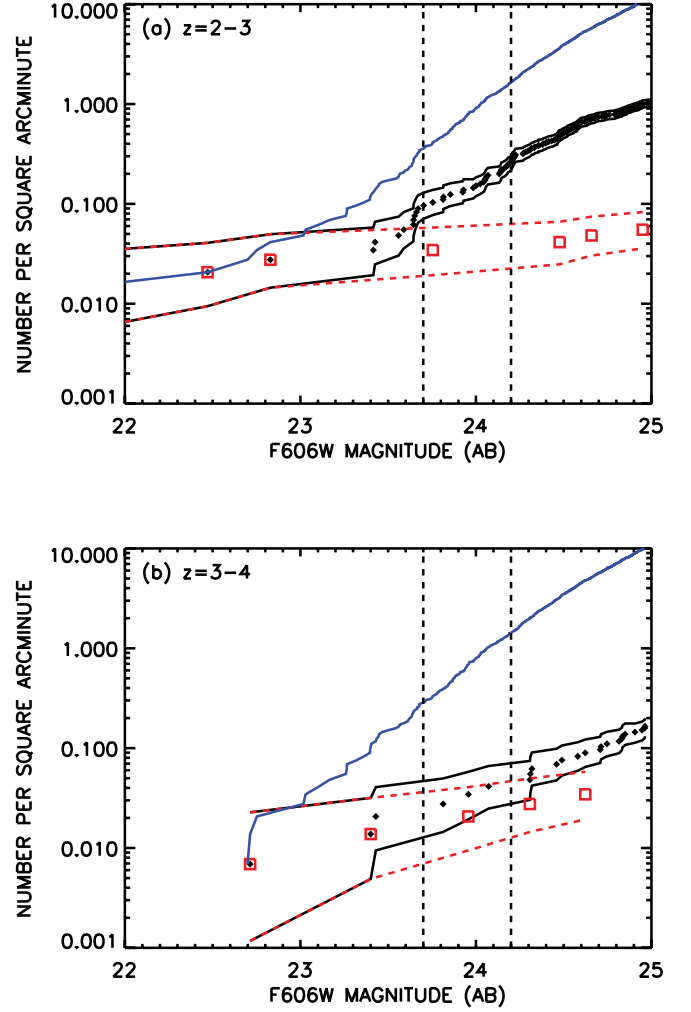

FIG. 17.—Cumulative surface densities of sources (galaxies and AGNs) in the ACS GOODS-N field vs. $F606W_{AB}$ magnitude for the redshift intervals (*a*) $z = 2–3$ and (*b*) $z = 3–4$ (*black diamonds with black solid curves for the 1 σ uncertainties*). AGNs alone are shown with red open squares. The red dashed curves in (*a*) show the 1 σ uncertainties for the AGNs. The maximum surface densities for the two redshift intervals are obtained by placing all of the spectroscopically unidentified sources into each redshift interval (*blue curves*). The black vertical dashed lines show the F606W AB magnitudes (24.2 and 23.7, respectively, for S/N per resolution element values of 20 and 30).

dashed curves). We obtain maximum surface densities by putting all of the spectroscopically unidentified sources into each redshift interval (*blue curves*).

We can see from Figure 17*a* that at magnitudes significantly brighter than $F606W_{AB} = 23.7$ the cumulative surface densities are still dominated by AGNs, and it is only near $F606W_{AB} = 24$ that galaxies begin to dominate. After allowing for the maximum possible correction in each redshift interval, the upper bound on the surface densities is $\lesssim 1.5$ arcmin^{-2} at $F606W_{AB} = 24.2$ (S/N = 20) in both the $z = 2–3$ and $z = 3–4$ ranges. This is an extreme upper limit, since the unidentified galaxies will not all lie in an individual redshift range and many may lie below $z = 2$. At $F606W_{AB} = 23.7$ (S/N= 30) the upper bound on the surface densities in both the $z = 2–3$ and $z = 3–4$ ranges is $\lesssim 0.4$ arcmin^{-2}. Again, this is an extreme upper limit, and the true value may be closer to the measured source value of 0.1 arcmin^{-2} in the $z = 2–3$ range. For a 10 m telescope the limiting magnitudes are 1.2 mag brighter, which means the surface densities that can be

observed with a 30 m telescope are a factor of $5-20$ higher than those that can be achieved with a 10 m telescope (e.g., 0.02 arcmin^{-2} at F606W$_{AB}$ = 22.5 for $z = 2-3$ and S/N= 30).

We conclude that with a 30 m telescope it will be possible to study examples of near neighbors and to map regions at arcminute scales. However, tomography at the subarcminute level is probably still beyond the reach of even an ideal 30 m telescope.

6. SUMMARY

In this paper we presented deep K_s-band imaging and the most spectroscopically complete redshift sample obtained to date of the 145 arcmin^2 *HST* ACS GOODS-N region. We provided the data in a variety of tables as a function of magnitude from the NUV to the MIR. The redshift identifications are greater than 90% complete to magnitudes of F435W$_{AB}$ = 24.5, F850LP$_{AB}$ = 23.3, and $K_{s,\,AB}$ = 21.5 and to 24 μm fluxes of 250 μJy.

We used the data to analyze various color selection techniques that have been proposed to find high-redshift galaxies. The LBG technique still appears to be the most robust method for providing a high selection completeness with low contamination. We do not confirm the presence of additional luminous galaxies not picked out by the LBG selection, as proposed by Le Fèvre et al. (2005). BzK, H$^-$, and IRAC color techniques can be highly efficient at selecting high-redshift ($z > 1.4$, $z > 1.3$, and $z > 1.6$, respectively) galaxies and AGNs but at the expense of a fairly high degree of contamination by lower redshift galaxies. Samples selected using these techniques therefore need to be spectroscopically followed up in order to obtain clean high-redshift samples.

Finally, we have used the ACS images to make detailed calculations of the S/N that can be obtained with spectral resolution 6000 seeing-limited spectra on a 30 m telescope. We find that spectra with S/N $\geq$ 30 per resolution element in 10 hr integ-

rations can only be obtained for galaxies brighter than F606W$_{AB}$ = 23.7. We have also computed the observed cumulative surface densities of galaxies and AGNs as a function of magnitude in the $z = 2-3$ and $z = 3-4$ ranges, as well as the maximum surface densities that could lie in these intervals when unidentified sources are included. These surface densities suggest that moderate spectral resolution (6000) observations with S/N $\geq$ 30 on a 30 m telescope will still primarily be of the AGN population and that the samples will be sparse with average separations greater than 1′ at $z = 2-4$.

REFERENCES

Abraham, R. G., et al. 2004, AJ, 127, 2455
Adelberger, K. L., Steidel, C. C., Shapley, A. E., Hunt, M. P., Erb, D. K., Reddy, N. A., & Pettini, M. 2004, ApJ, 607, 226
Alexander, D. M., et al. 2003, AJ, 126, 539
Alonso-Herrero, A., et al. 2006, ApJ, 640, 167
Angeli, G., & Roberts, S., eds. 2007, TMT Observatory Requirements Document 2007 (TMT.SEN.DRD.05.001.CCR18; Pasadena: TMT)
Barger, A. J., Cowie, L. L., & Wang, W.-H. 2007, ApJ, 654, 764
Barger, A. J., et al. 2003, AJ, 126, 632
Barmby, P., et al. 2006, ApJ, 642, 126
Bertin, E., & Arnouts, S. 1996, A&AS, 117, 393
Bruzual, G., & Charlot, S. 2003, MNRAS, 344, 1000
Capak, P., et al. 2004, AJ, 127, 180
Cardamone, C. N., et al. 2008, ApJ, 680, 130
Chapman, S. C., Blain, A. W., Smail, I., & Ivison, R. J. 2005, ApJ, 622, 772
Chapman, S. C., Smail, I., Blain, A. W., & Ivison, R. J. 2004, ApJ, 614, 671
Cimatti, A., et al. 2002, A&A, 392, 395
Cohen, J. G. 2001, AJ, 121, 2895
Cohen, J. G., et al. 2000, ApJ, 538, 29
Condon, J. J. 1992, ARA&A, 30, 575
Cowie, L. L., & Barger, A. J. 2008, ApJ, 686, 72
Cowie, L. L., Barger, A. J., Hu, E. M., Capak, P., & Songaila, A. 2004, AJ, 127, 3137
Cowie, L. L., Barger, A. J., & Trouille, L. 2008, ApJ, in press
Cowie, L. L., Lilly, S. J., Gardner, J., & McLean, I. S. 1988, ApJ, 332, L29
Cowie, L. L., Songaila, A., Hu, E. M., & Cohen, J. G. 1996, AJ, 112, 839
Daddi, E., Cimatti, A., Renzini, A., Fontana, A., Mignoli, M., Pozzetti, L., Tozzi, P., & Zamorani, G. 2004, ApJ, 617, 746
Daddi, E., Dannerbauer, H., Elbaz, D., Dickinson, M., Morrison, G., Stern, D., & Ravindranath, S. 2008, ApJ, 673, L21
Dawson, S., Stern, D., Bunker, A., Spinrad, H., & Dey, A. 2001, AJ, 122, 598
Donley, J. L., Rieke, G. H., Pérez-González, P. G., Rigby, J. R., & Alonso-Herrero, A. 2007, ApJ, 660, 167
Elvis, M., et al. 1994, ApJS, 95, 1
Epps, H., & Miller, J. S. 1998, Proc. SPIE, 3355, 48
Faber, S. M., et al. 2003, Proc. SPIE, 4841, 1657

Fazio, G., et al. 2004, ApJS, 154, 10
Franx, M., et al. 2003, ApJ, 587, L79
Giavalisco, M., et al. 2004, ApJ, 600, L93
Grazian, A., et al. 2007, A&A, 465, 393
Hatziminaoglou, E., et al. 2005, AJ, 129, 1198
Hawarden, T. G., Leggett, S. K., Letawsky, M. B., Ballantyne, D. R., & Casali, M. M. 2001, MNRAS, 325, 563
Jenkins, E. B. 1986, ApJ, 304, 739
John, T. L. 1988, A&A, 193, 189
Kajisawa, M., et al. 2006, PASJ, 58, 951
Kong, X., et al. 2006, ApJ, 638, 72
Krisciunas, K. 1997, PASP, 109, 1181
Lacy, M., et al. 2004, ApJS, 154, 166
Lane, K. P., et al. 2007, MNRAS, 379, L25
Le Fèvre, O., et al. 2005, Nature, 437, 519
Lilly, S. J., Cowie, L. L., & Gardner, J. 1991, ApJ, 369, L79
Lowenthal, J. D., et al. 1997, ApJ, 481, 673
Martin, D. C., et al. 2005, ApJ, 619, L1
Moran, E. C., Lehnert, M. D., & Helfand, D. J. 1999, ApJ, 526, 649
Neugebauer, G., Oke, J. B., Becklin, E. E., & Matthews, K. 1979, ApJ, 230, 79
Oke, J. B., et al. 1995, PASP, 107, 375
Paltani, S., et al. 2007, A&A, 463, 873
Papovich, C. 2008, ApJ, 676, 206
Patat, F. 2003, A&A, 400, 1183
Phillips, A. C., Guzman, R., Gallego, J., Koo, D. C., Lowenthal, J. D., Vogt, N. P., Faber, S. M., & Illingworth, G. D. 1997, ApJ, 489, 543
Pope, A., et al. 2008, ApJ, 675, 1171
Popesso, P., et al. 2008, A&A, in press (arXiv:0802.2930)
Prochaska, J. X. 2006, ApJ, 650, 272
Quadri, R., et al. 2007, ApJ, 654, 138
Reddy, N. A., Erb, D. K., Steidel, C. C., Shapley, A. E., Adelberger, K. L., & Pettini, M. 2005, ApJ, 633, 748
Reddy, N. A., Steidel, C. C., Erb, D. K., Shapley, A. E., & Pettini, M. 2006, ApJ, 653, 1004
Richards, E. A. 2000, ApJ, 533, 611
Rieke, G., et al. 2004, ApJS, 154, 25

Sajina, A., Lacy, M., & Scott, D. 2005, ApJ, 621, 256

Sawicki, M. 2002, AJ, 124, 3050

Sheinis, A. I., Miller, J. S., Bolte, M., & Sutin, B. M. 2000, Proc. SPIE, 4008, 522

Silva, D., Hickson, P., Steidel, C. C., & Bolte, M., eds. 2007, in Thirty Meter Telescope Detailed Science Case (TMT.PSC.TEC.07.003.REL01; Pasadena: TMT)

Simpson, C., & Eisenhardt, P. 1999, PASP, 111, 691

Songaila, A., Cowie, L. L., & Lilly, S. J. 1990, ApJ, 348, 371

Steidel, C. C., Adelberger, K. L., Giavalisco, M., Dickinson, M, & Pettini, M. 1999, ApJ, 519, 1

Steidel, C. C., Adelberger, K. L., Shapley, A. E., Pettini, M., Dickinson, M., & Giavalisco, M. 2003, ApJ, 592, 728

Steidel, C. C., Giavalisco, M., Pettini, M., Dickinson, M., & Adelberger, K. L. 1996, ApJ, 462, L17

Steidel, C. C., & Hamilton, D. 1993, AJ, 105, 2017

Steidel, C. C., Pettini, M., & Hamilton, D. 1995, AJ, 110, 2519

Steidel, C. C., Shapley, A. E., Pettini, M., Adelberger, K. L., Erb, D. K., Reddy, N. A., & Hunt, M. P. 2004, ApJ, 604, 534

Stern, D., et al. 2005, ApJ, 631, 163

Swinbank, A. M., Smail, I., Chapman, S. C., Blain, A. W., Ivison, R. J., & Keel, W. C. 2004, ApJ, 617, 64

Tokunaga, A. T., Simons, D. A., & Vacca, W. D. 2002, PASP, 114, 180

Treister, E., et al. 2006, ApJ, 640, 603

Treu, T., Ellis, R. S., Liao, T. X., & van Dokkum, P. G. 2005, ApJ, 622, L5

Trouille, L. T., Barger, A. J., Cowie, L. L., Yang, Y., & Mushotzky, R. F. 2008, ApJS, 179, 1

van Dokkum, P. G., et al. 2003, ApJ, 587, L83

Wirth, G. D., et al. 2004, AJ, 127, 3121

Zezas, A. L., Georgantopoulos, I., & Ward, M. J. 1998, MNRAS, 301, 915